CATALYSIS WITH TITANIA-SUPPORTED PALLADIUM FOR AMMONIA-CAPTURED

CO$_2$-BASED BICARBONATE-FORMATE LIQUID ORGANIC HYDROGEN CARRIER

By

AHMAD MUKHTAR

A thesis submitted in partial fulfillment of
the requirements for the degree of

MASTER OF SCIENCE IN CHEMICAL ENGINEERING

WASHINGTON STATE UNIVERSITY
Gene and Linda Voiland School of Chemical Engineering and Bioengineering

JULY 2023

To the Faculty of Washington State University:

The members of the Committee appointed to examine the thesis of AHMAD MUKHTAR find it satisfactory and recommend that it be accepted.

<div style="text-align: right">

_____

Hongfei Lin, Ph.D., Chair

_____

Yong Wang, Ph.D.

_____

David Jacob Heldebrant, Ph.D.

_____

Mark Bowden, Ph.D.

</div>

CATALYSIS WITH TITANIA-SUPPORTED PALLADIUM FOR AMMONIA-CAPTURED

CO_2-BASED BICARBONATE-FORMATE LIQUID ORGANIC HYDROGEN CARRIER

Abstract

by Ahmad Mukhtar, M.S.
Washington State University
July 2023

Chair: Hongfei Lin

Developing next-generation heterogeneous catalysts for efficient bicarbonate-formate systems is necessary for economical and environmentally friendly CO_2-assisted hydrogen energy. The development of highly efficient heterogeneous catalysts without compromising on stability is still a challenging task. In this work, we synthesized the palladium (Pd) supported over titania (TiO_{2-x}). The catalysts were subjected to electronic structure, geometric, and adsorption strength-based characterizations. The catalyst was evaluated for (ammonium)bicarbonate-formate (de)hydrogenation system kinetics and stability. The results revealed a synergistic effect of the hydrogen spillover and oxygen vacancies in enhancing catalyst activity. The oxygen vacancies were supposed to mobilize and stabilize the intermediate species, whereas the electron transfer from TiO_2 to Pd was observed, creating strong metal-support interactions. The active sites were identified, and a possible mechanism for the (ammonium)bicarbonate-formate (de)hydrogenation system was suggested. The computational study investigated the electron mobility and binding energies of different species with and without oxygen vacancies.

TABLE OF CONTENTS

LIST OF TABLES

CHAPTER 1: INTRODUCTION AND BACKGROUND

1.1. Why Transition from Fossil Fuels to Renewable Energy?

It is an admitted fact that the destiny of humankind is now at a cross-road where the generation of economic wealth through technological progress resulted in the bypassing of general laws of nature exceeding the capabilities of our planet [1-3]. We also acknowledge that the greatest minds in science taught us how to master the application of fire by burning fossil fuels to run the machines to do work for us. Considering the concept of the 4.0 industry, we can say that we are at the edge where the machines mentioned above are closer to extending their capabilities toward artificial intelligence (AI). However, such idea of further technological advances to generate wealth and equal rights across the globe remains a debate to date [4]. Unfortunately, despite all of the technological developments, humankind is still unsuccessful in identifying and recognizing our current enterprise's limits. This enterprise includes the amount of natural resources available to us. We are cruelly lacking the leadership with the imagination to reinvent the society-based organization and develop models to cope with the challenges we are facing now and in the future.

Regarding possible solutions, some people demand the degrowth of the economies followed by the reorganization of the currently implemented economic models. However, this is only one aspect of the proposed solution [5]. Considering the global emerging economies, the current energy demand is subjected to double to support economic development. Hence, the availability of vast amounts of energy globally is readily demanding. Indeed, our access to energy directly correlates with the quality of life and the viability of the currently employed economic models [6].

On the other hand, it is unfortunate that most of the energy produced across our planet is consumed by a minority fraction of the world population. One possible and long-term solution to the fairness of energy distribution and consumption can be achieved by renewable energy, that can be accessible across the planet but not possible through the utilization of fossil fuels where some selected nations are considered fossil fuel rich. Taking photovoltaic technology as an example which can easily support around 10 billion people for their energy needs [7]. Nonetheless, developing efficient energy carriers is one of the major hindrances to commercializing renewable energy technology. Renewable energy sources are considered intermittent, while our society depends on dispatchable energy ready for their use 24/7. It could be achieved by using renewable energy to produce synthetic hydrocarbons locally. However, overall efficiency will remain low. Considering the concept of decarbonized economies, the employment of hydrogen as an alternative energy carrier (**Figure 1.1**) is a more viable option compared to others [8, 9].
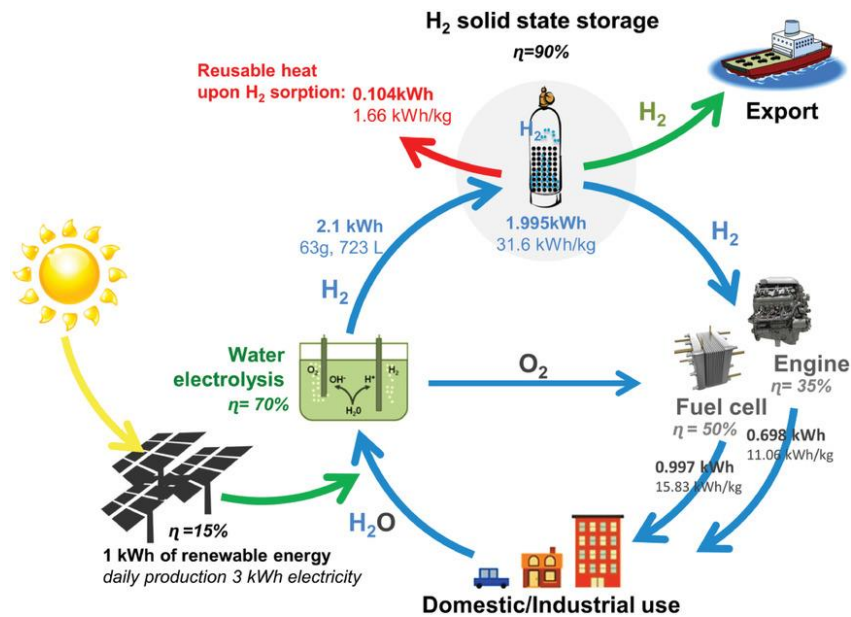
Figure 1.1. Schematic illustration of the hydrogen economy in terms of renewable hydrogen supply chain. Reprinted from the reference [1] with the permission of the Wiley.

Hydrogen has 3 times higher gravimetric energy density compared to conventional gasoline. Compared to traditional fossil fuels, hydrogen is abundant. It can be produced via water splitting and used for various energy-related applications such as fuel cell-based electricity production, combustion engines-based mechanical work, and catalytic combustion-based heat generation. We know that the idea of replacement of conventional fossil fuel with hydrogen is not new. Still, this idea has been subjected to a series of stop-and-go policies that have left the impression that this technology is not mature [10].

1.2. CO_2 Emissions

The exploitation of traditional energy resources has become seriously problematic due to the ever-increasing demand for energy and its direct contribution to greenhouse gas emissions leading to the global climate crisis except some global events in last century to date where we observed a decline in CO_2 emissions for a short period of time (**Figure 1.2**, Right). It is well known that in the last century, the development in the culture, economy, and science and technology resulted in the utilization of traditional energy resources, i.e., fossil fuels, for the gain of energy but at the same time their extended utilization resulted in serious environmental problems such as the global climate change, i.e., an increase in the temperature of the earth. Such issues urgently demand transitioning from traditional fossil fuel-based energy resources to renewable and carbon-free ones (**Figure 1.2**, Left). In 2015, an agenda known as the "2030 Agenda for Sustainable Development" was approved and adopted by the United Nations (UN) to reduce the consumption of traditional energy resources, i.e., fossil fuels, for the gain of energy with an efficient circular economy-based approach. The final goal of the adopted agenda was to reduce the impact of the traditional energy resources-related adverse effects on health, security, safety, and the environment [11]. The center of sustainable development aims to design a green future based on the transition

3

from traditional energy resources, i.e., fossil fuels, to renewable energy resources [12]. In the search for renewable energy resources, biomass is found to be renewable, natural, abundant, and carbon-neutral. At the same time, its use also provides a promising alternative to traditional energy resources, i.e., fossil fuels. It can be used in the commercial scale production of fuels, chemicals, and materials, other than energy generation [13-23]. However, the major obstacle associated with biomass as a renewable energy resource is that when we use biomass for large-scale production of fuel, the cost-effectiveness and process efficiencies are not comparable to the traditional energy resources, i.e., fossil fuels [24]. Compared to biomass, hydrogen energy in terms of the liquid organic hydrogen carriers (LOHCs), which can be integrated with CO_2 capture and utilization, is a promising alternative [25].
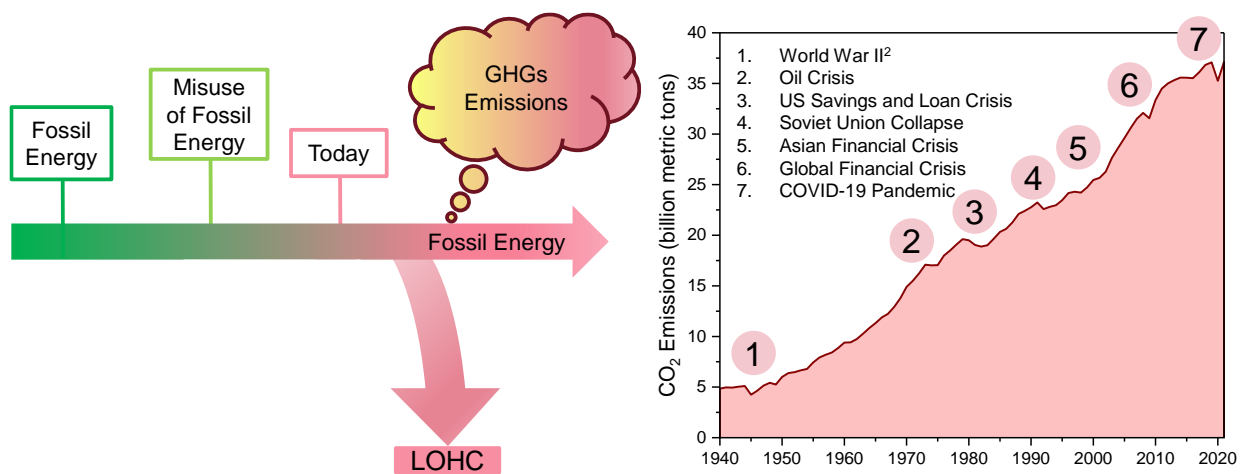
Figure 1.2. *(Left):* A schematic illustration of a journey leading to misuse of fossil fuels and its transformation to liquid organic hydrogen carriers (LOHCs), *(Right):* Trend of global CO_2 emissions during 1940 – 2020.

(Left): Reproduced from the reference [25] with the permission of Wiley and *(Right):* Reproduced from the reference [26] with the permission of Nature Publishing Group.

1.3. Liquid Organic Hydrogen Carriers (LOHCs)

As in the preceding section, we discussed that hydrogen has been identified as a potential alternative and clean energy source to traditional energy resources, i.e., fossil fuels. Hydrogen can be produced in several ways, including electrolysis-based water splitting, steam reforming, coal gasification, and the partial oxidation of hydrocarbons. However, only the production of hydrogen is not sufficient for the implementation of the hydrogen-based economy. Developing cost-effective and energy-efficient hydrogen storage, transport, and delivery for a hydrogen-based economy is of critical significance [27-29]. In this regard, several hydrogen storage technologies have been developed for storage, transport, and delivery. These technologies include adsorption, compression, liquefaction, chemisorption, adsorption, chemical reactions, etc. [30]. Selecting a suitable technology for hydrogen storage involves considering a number of factors (**Figure 1.3**, Right). A comparison of the gravimetric and volumetric densities for the hydrogen mentioned above storage technologies is tabulated in (**Table 1.1**) [28, 30-32].

Table 1.1. Comparison of different hydrogen storage technologies [28, 30-32].

H$_2$ Storage Technology	Gravimetric Density (kg H$_2$/kg)	Volumetric Density (kg H$_2$/m^3)	Operating Pressure (MPa)	Operating Temperature (K)
Compression	3-4.8	17-33	35-70	Ambient
Liquefaction	6.5-14	35-40	0.10	20
Adsorption on Activated Carbon	5-7	20-30	5-10	77
Low – Temperature Hydrides	2-3	<120	0.1-3	Ambient
High – Temperature Hydrides	3-8	<150	0.1-1	<373

Chemical Hydrides	3-5	20-30	1	350-473
LOHCs	4.5-7.2	70	0.1	Ambient

The LOHCs are considered an exciting and promising option compared to these technologies. One of the key advantages of the LOHCs is hydrogen storage, transport, and delivery in ambient conditions. The concept of LOHCs is based on the reversible hydrogenation – dehydrogenation cycles (**Figure 1.3**, Left).
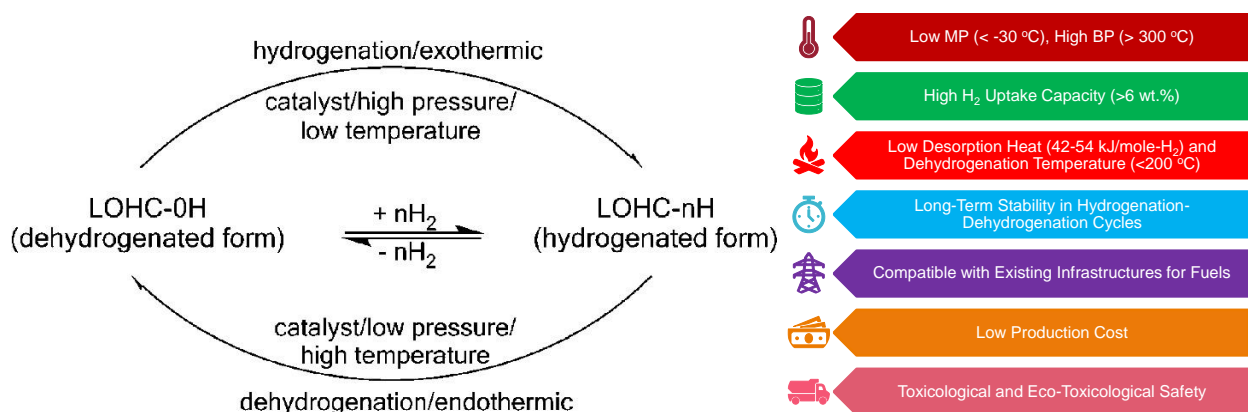
Figure 1.3. *(Left):* Schematic illustration of the concept of LOHCs. Reprinted from the reference [27] with the permission of the American Chemical Society and *(Right):* Key characteristics of an ideal LOHCs [33].

In the hydrogen storage step, the LOHCs, i.e., an organic compound, are hydrogenated at elevated pressure and low temperature to store hydrogen and convert it into a corresponding saturated compound in the presence of a catalyst [31, 34-38]. This saturated compound, considered to be hydrogen-rich, can be transported to the place of energy demand, where it can be dehydrogenated in the presence of a catalyst at higher temperatures and low pressure to release the hydrogen. After dehydrogenation, the saturated compounds convert to the original compound and

are ready for the next hydrogenation cycle. Key characteristics of an ideal LOHCs are presented in (**Figure 1.3**, Right).

1.4. Integrated CO_2 Capture and Utilization

It is well admitted that the CO_2 capturing and utilization (CCU) results in additional costs associated with the desorption of CO_2 from the capturing agent, purification, followed by the compression step to transport the CO_2 to the utilization facility (**Figure 1.4**, Left). To avoid these costs and make the overall process cost-effective, the researchers are more endeavored towards the integrated CO2 capture and utilization (ICCU), which skips the additional cost mentioned above. ICCU enables in one step, i.e., in-situ CO_2 capture and its utilization or conversion to fuel-graded and valuable products. Formic acid/formate salts and methanol are the dominant products produced by the ICCU as they have a leading role in fuel and hydrogen storage [39-42]. In this regard, we have divided the ICCU system into four categories depending on the material used for CO_2 capturing and the product formed during that process (**Figure 1.4**, Right). For example, first, the CO_2 capturing by the amine solution converts into the carbamate and/or bicarbonates and subsequent hydrogenation to alkylammonium formate salts. Second, it is like the first category of CO_2 capturing, converting to fuel-graded methanol via hydrogenation at a different CO_2:H_2 ratio and reaction conditions. Third, it involves the capturing of CO_2 with some hydroxide bases such as the aqueous ammonia, i.e., ammonium hydroxide (NH_4OH) as carbonate/bicarbonate/carbamate depending on the system pH and subsequent conversion to formate salts such as ammonium hydroxide which serve as a liquid organic hydrogen carrier in our study. Fourth, it is like the third category up the CO_2 capturing while its subsequent conversion to methanol is not reported widely.

7

Like formic acid (FA), the various formate salts or derivatives could be employed as the LOHCs. It has been found that only a few catalyst developments have been reported for FA due to its strong acidic conditions. However, the formate salts are a better replacement for FA as LOHCs due to their non-volatile, non-corrosive, non-toxic, and non-acidic nature, providing a convenient reaction medium. It has been found that the hydrogen release from the formate salts is not as favorable as in the case of FA, i.e., ($\Delta G = 1$ kJ/mole for formate salts, Na^+, K^+, and NH_4^+ while $\Delta G = -32.9$ kJ/mole for FA). However, the hydrogen release from the formate salts is neither exergonic nor endergonic, which makes the bicarbonate – formate-based LOHCs system thermodynamically favorable at ambient conditions [43].

Our previous research [44] reported that by using Pd/C catalyst, the ammonium bicarbonate has better hydrogen storage capacity than other bicarbonate salts, such as sodium bicarbonate, under identical reaction conditions. It is because the cations of the bicarbonate salts might shift the equilibrium between the carbonate or bicarbonate ions. Based on ^{13}C – Nuclear Magnetic Resonance (NMR) results, it has been found that the ammonium bicarbonate has higher concentrations of HCO_3^{-1} than CO_3^{-2} leading to ion pair shifts peaks (155 to 170 ppm) to lower ppm values confirming the higher hydrogen storage of ammonium bicarbonates compared to other salts. From the hydrogen release aspect, similar results were observed. The ammonium formate yielded a 63% yield at a temperature of 80 °C and reaction time of 20 mins compared to the sodium formate, which produced a 44% yield at identical reaction conditions. The H_2 evolution efficiency of the conjugate acid ion, NH_4^+, is much higher than the H_2 evolution from H_2O in the case of sodium formate.

One of the significant concerns in employing the (ammonium)bicarbonate-formate salts for hydrogen storage and release is their corresponding solubility limits. At room temperature, ammonium formate has higher solubility (~22 mol/L) than ammonium bicarbonate which has a very low solubility (~3 mol/L). Another concern is the thermal instability of ammonium bicarbonate at higher temperatures. The ammonium bicarbonate decomposes into carbon dioxide (CO_2) and ammonia (NH_3) at temperatures above 35 $^\circ$C. These factors, including the low solubility and thermal instability, restrict the higher concentration of ammonium bicarbonate, leading to lower hydrogen storage capacity.
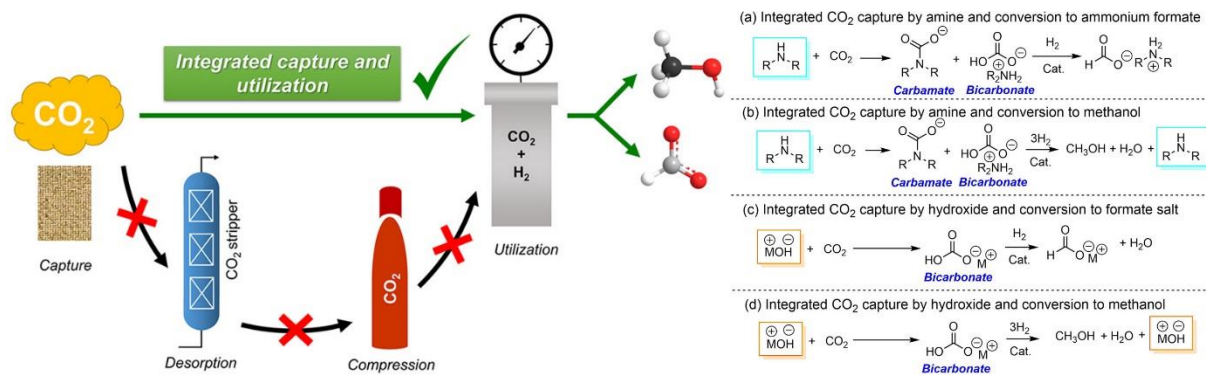
Figure 1.4. *(Left):* A schematic illustration of benefits of integrated CO_2 capture and utilization (ICCU) compared to CO_2 capture and utilization (CCU), *(Right):* Possible ways for the ICCU to fuel-graded and value-added products. Reprinted from the reference [39] with the permission of the American Chemical Society.

1.5. Catalysis for CO_2 – Formic Acid Systems

Since CO_2 is the leading greenhouse gas contributing to climate change, it has been considered one of the attractive alternatives for reversible hydrogen storage and delivery options compared to the nitrogen – ammonia couple. It is well known that the hydrogenation of CO_2 could easily yield the C1 products, which include formaldehyde, formic acid, methane, and methanol. The advantage

of CO_2 – formic acid-based reversible hydrogen storage and delivery cycle is that the formic acid and its subsequent salts are readily available. One of the drawbacks of the CO_2 – formic acid-based reversible hydrogen storage and the delivery cycle is that during the hydrogen delivery phase, i.e., formic acid decomposition results in carbon monoxide (CO). This unwanted byproduct can poison the most utilized noble metal, i.e., Pd-based heterogeneous catalysts, and hamper the extension of this idea towards fuel cell applications [45, 46]. From a thermodynamic point of view, CO_2 hydrogenation to formic acid seems thermodynamically unfavorable if the reaction occurs without any base or solvent in the gas phase. However, when the reaction is performed in the presence of a solvent such as water or base, the reaction becomes exergonic, probably due to the dissolution of gases. A stronger trend is observed in later cases, i.e., base use [47]. On the other hand, the delivery of hydrogen via the thermocatalytic decomposition of formic acid is thermodynamically favored; however, there is a need to compete with the dehydration reaction, which produces CO [46]. A summary of the Gibbs free energy of reactions associated with the CO_2 – HCOOH – based reversible hydrogen storage and delivery system are tabulated in (**Table 1.2**).

Table 1.2. Thermodynamics of CO_2 – HCOOH – based reversible hydrogen storage and delivery system [47].

Equation No.	Reactions	Gibbs Free Energy (ΔG_{298K}, kJ/mole)
1	CO_2 (g) + H_2 (g) → HCOOH (l)	+32.9
2	CO_2 (aq.) + H_2 (aq.) → HCOOH (l)	-4
3	HCOOH (l) → CO_2 (g) + H_2 (g)	-32.9
4	HCOOH (l) → CO (g) + H_2O (l)	-12.4

Lee et al. [48] developed an innovative process to immobilize the palladium (Pd) nanoparticles over the mesoporous graphitic carbon nitride support (mpg-C_3N_4) for H_2 production from formic acid. The results revealed that the small-sized Pd/mpg-C_3N_4 demonstrated excellent activity in H_2 production originating from the high concentrations of the nitrogen functionalities (**Figure 1.5**). These nitrogen functionalities played a significant role in the stabilization of Pd nanoparticles as well as providing the basic sites for the activation of formic acid. Additionally, it was found that the Pd/mpg-C_3N_4 was found to be active in the synthesis of formic acid via CO_2 hydrogenation in the presence of a solvent, i.e., triethylamine (TEA). The basic site of the support provides an initial interaction for the CO_2 for its hydrogenation to formic acid. Bi et al. [49] reported the advanced catalyst based on the Pd supported on pyridinic nitrogen-doped carbon for the CO_2 – Formic acid-based reversible LOHC. They found that the controlled synthesis strategy helped to optimize the electronic conditions of the Pd/CN_X catalyst to enhance the activity for formic acid synthesis and H_2 production with the assistance of pyridinic functional groups (**Figure 1.5**).
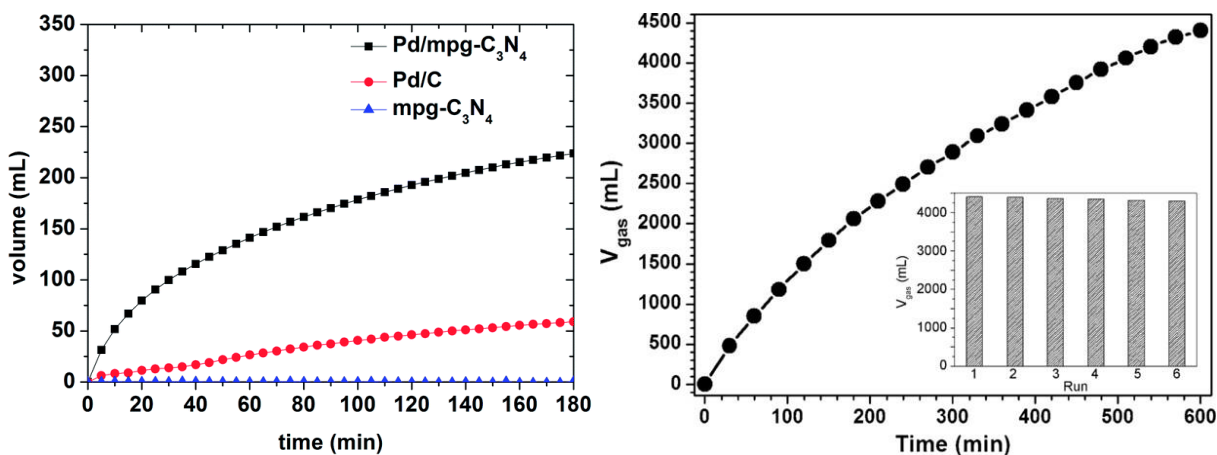
Figure 1.5. *(Left):* Formic acid dehydrogenation to produce H_2 over mpg-C_3N_4, Pd/C, and Pd/mpg-C_3N_4.

Reaction Conditions: support/catalyst loading (50 mg), formic acid (1M, 10 mL), and temperature 25 °C. Reprinted from the reference [48] with the permission of the Royal Society of Chemistry. *(Right):* H_2 production at large scale from formic acid over the $Pd/CN_{0.25}$ catalyst. Reaction Conditions: Pd loading (75.4 µmole), formic acid (1M, 100 mL), reaction time (600 minutes), and temperature 25 °C. Reprinted from the reference [49] with the permission of Wiley.

However, both studies reported the 5-6 cycles of catalyst recycling in dehydrogenation. The catalyst stability was not investigated in hydrogenation which is critical for the catalyst development and deployment for the liquid organic hydrogen carriers (LOHCs).

In another work, Mori et al. [50] reported the nitrogen-modified mesoporous silica (SBA-15) supported Pd nanoparticles for the interconversion reaction between CO_2 and formic acid (**Figure 1.6**). The catalyst efficiently produced formic acid from CO_2 hydrogenation and H_2 from formic acid dehydrogenation. The catalyst activity was optimized by tuning the electronic configuration using a guest metal silver (Ag) to synthesize bimetallic catalysts. The Pd:Ag ratio was changed to optimize the electronic state and activity towards the interconversion reaction between CO_2 and formic acid. The catalyst stability was not investigated in this work.

In a similar work, Masuda et al. [51] reported the synthesis of bimetallic catalysts based on Pd and Ag supported on the nitrogen-functionalized mesoporous carbon (MSC-Amine) where nitrogen functionalities were incorporated using the phenylamine (**Figure 1.7**). The catalysts were tested for chemical hydrogen storage, i.e., interconversion reaction between the CO_2 and formic acid. It was found that the functionalization of support with nitrogen functionalities assisted in dispersing the PdAg nanoparticles, and together with guest metal Ag, the electronic structure was

optimized to enhance the catalyst activity for interconversion reaction between the CO_2 and formic acid.
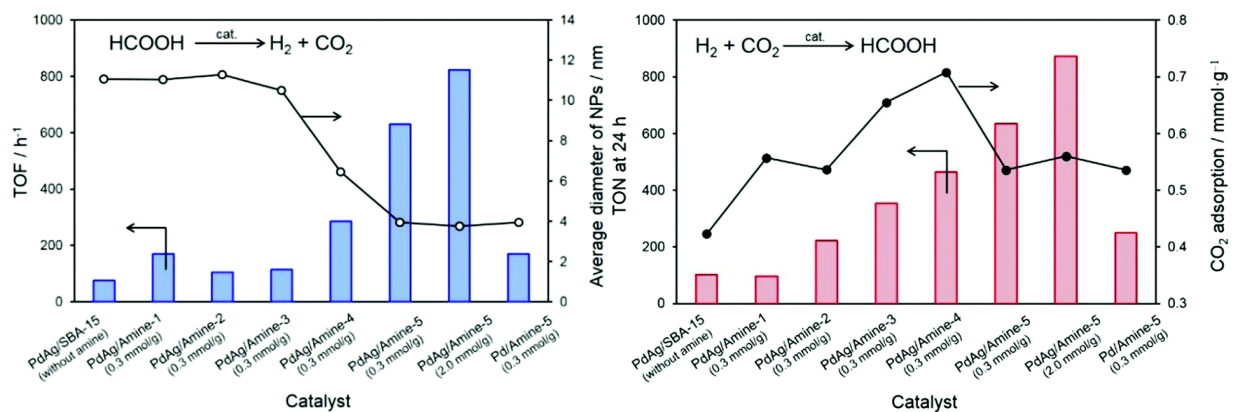
Figure 1.6. Interconversion reaction between the CO_2 and formic acid over Pd/SBA-15-Amine and PdAg/SBA-15-Amine catalysts.

Reaction Conditions: *(Dehydrogenation, Left):* catalyst loading (0.1 g), HCOONa/HCOOH (1M, 10 mL, 1/9), temperature 348 K, and Ar atmosphere. *(Hydrogenation, Right):* catalyst loading (0.05 g), $NaHCO_3$ (1M, 10 mL), total pressure (2.0 MPa, $CO_2:H_2$ 1:1), and temperature 373 K. Reprinted from the reference [50] with the permission of the Royal Society of Chemistry.

A combined experimental and density functional theory (DFT) based study revealed that the nitrogen functionalities positively impact the dissociation of O-H bonds during the H_2 production by the dehydrogenation of formic acid. Additionally, the interaction between the nitrogen functionalities, i.e., phenylamine molecules, stabilized the bicarbonate (HCO_3^-)-based intermediate species during the hydrogenation of CO_2. The catalyst was employed for stability testing in the interconversion reaction between CO_2 and formic acid. It was found to maintain the activity for 3 cycles in hydrogenation and dehydrogenation (**Figure 1.7**) separately.
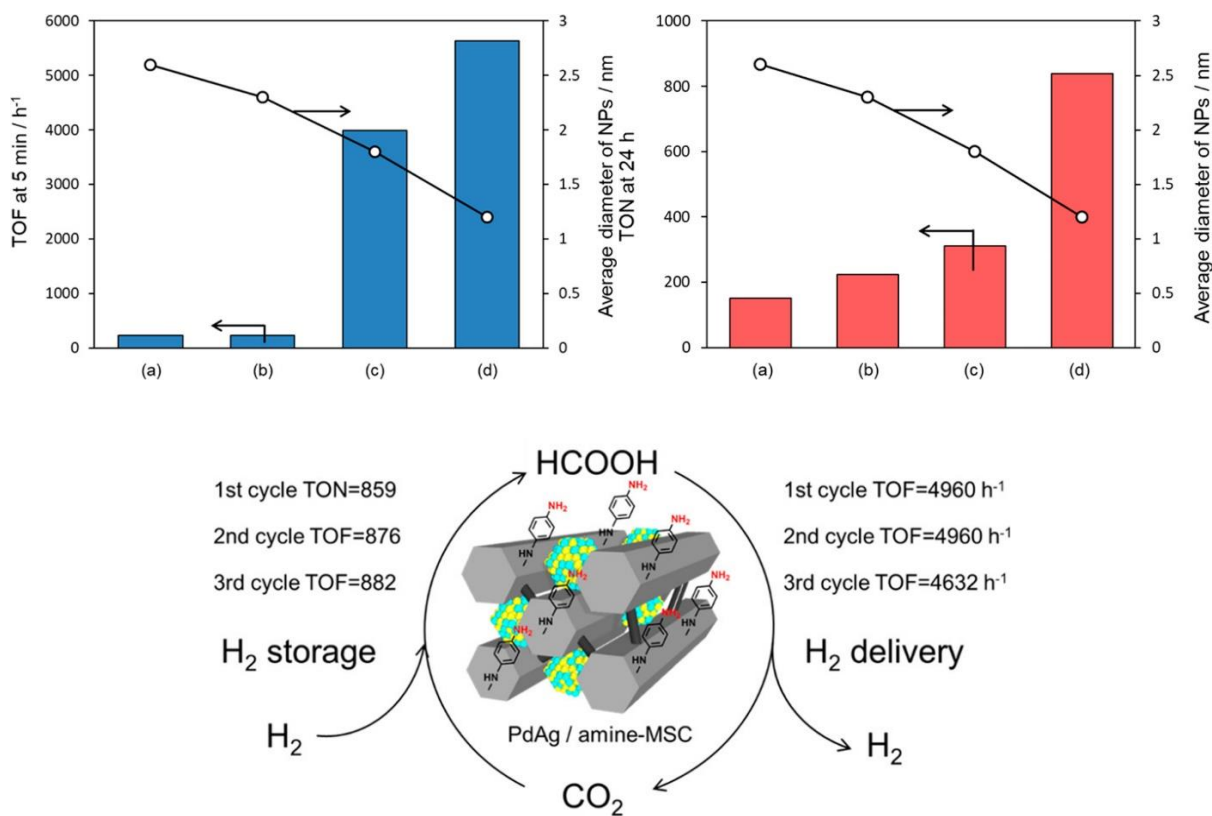
Figure 1.7. *(Top):* Interconversion reaction between the CO_2 and formic acid over Pd/MSC-Amine catalysts, (a): Pd/MSC, (b): PdAg/MSC, (c): Pd/MSC-Amine, and (d): PdAg/MSC-Amine. *(Bottom):* Stability testing of Pd/SBA-15-Amine catalyst in the Interconversion reaction between the CO_2 and formic acid.

<u>Reaction Conditions:</u> *(Dehydrogenation, Top Left):* catalyst loading (0.05 g), HCOONa/HCOOH (0.3M, 10 mL, 1/9), temperature 348 K, reaction time (15 minutes), and Ar atmosphere. *(Hydrogenation, Top Right):* catalyst loading (50 mg), $NaHCO_3$ (1M, 10 mL), total pressure (2.0 MPa, CO_2:H_2 1:1), reaction time (24 hours), and temperature (100 °C). Reprinted from the reference [51] with the permission of the American Chemical Society.

In our previous work [52], our research group proposed a novel idea integrating CO_2 capturing with the LOHC concept. In a typical procedure, the CO_2 was captured using a piperidine

solvent and further subjected to hydrogenation over the Pd/C catalyst. The CO_2 was captured using the piperidine solvent in combination with the aqueous-alcoholic solvents. The results revealed that using piperidine as CO_2 capturing solvent in water-ethanol (30:70 wt.%), the subsequent hydrogenation yielded approximately 95.5% formate at an H_2 pressure of 400 psi for 1-hour reaction at 30 °C. The reversible reaction rate, i.e., the H_2 production from dehydrogenation reaction, was also found to be fast, and H_2 purity (ammonia and carbon monoxide free H_2) of 100% was obtained in 40 minutes reaction time at a temperature of 100 °C (**Figure 1.8**). Additionally, the mechanistic study by using the in-situ Attenuated total reflection – Fourier transform infrared spectroscopy (ATR – FTIR) characterization revealed that the utilization of piperidine solvent for CO_2 capturing improves both hydrogenation and dehydrogenation activities, and there was no detectable CO bound with the catalyst surface during the dehydrogenation reaction. It could be due to piperidine's ligand effect to enrich the Pd electron (**Figure 1.8**).
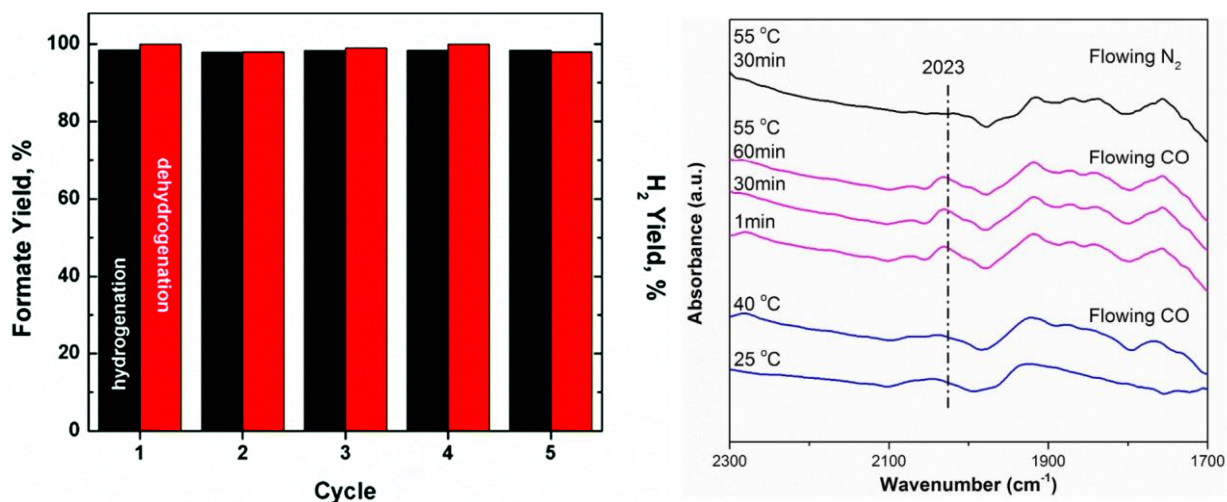
Figure 1.8. *(Left):* Stability testing of the Pd/C catalyst for the interconversion reaction between the CO_2 and formic acid over Pd/MSC-Amine catalysts, (a): Pd/MSC, (b): PdAg/MSC, (c):

Pd/MSC-Amine, and (d): PdAg/MSC-Amine. *(Right):* In-situ ATR – FTIR spectra of Pd/C with

flowing CO (pink lines).

Reaction Conditions: *(Dehydrogenation, Left):* 2-propanol (70 wt.%), catalyst loading (0.1 g),

HCOONa/HCOOH (0.3M, 10 mL, 1/9), temperature 100 °C, and reaction time (30 minutes).

(Hydrogenation, Left): 2-propanol (70 wt.%), catalyst loading (0.1 g), reaction time (1 hour), and

temperature (30 °C). *(In-situ ATR – FTIR, Right):* 5% Pd/C was coated on the window of ATR,

followed by a 10% CO balanced with helium flow at 20 mL/min through the ATR cell. The

temperature was raised from 25 °C to 55 °C maintained for 1 hour, and then nitrogen flow at 20

mL/min was introduced. Reprinted from the reference [52] with the permission of the Royal

Society of Chemistry.

Sun et al. [53] reported the synthesis of Pd and manganese (Mn) based bimetallic catalysts

caged in the zeolite support for the interconversion reaction between the CO_2 and formic acid.

They developed sub-nanometer Pd-Mn clusters encapsulated in the S-1 zeolites using in-situ

hydrothermal conditions with a ligand-protected strategy. The $PdMn_X@S-1$ demonstrated

excellent activity in the CO_2 hydrogenation to formic acid and H_2 release from the

dehydrogenation of formic acid (**Figure 1.9**). The excellent performance of the catalyst in the

interconversion reaction between the CO_2 and formic acid was directed to the ultrasmall and well-

dispersed Pd-Mn metal clusters and the synergy between Pd and Mn in terms of ligand effect, i.e.,

electron transfer effect. In combination with the experimental investigations, the DFT calculations

revealed that the alloying of Pd with the Mn resulted in a compact structure with electronic state

tuning that can help optimize the intermediate species' binding energies. The catalyst was stable

for 5 runs in hydrogenation and dehydrogenation reactions separately. A summary of the catalysts discussed in this section are tabulated in (**Table 1.3**).
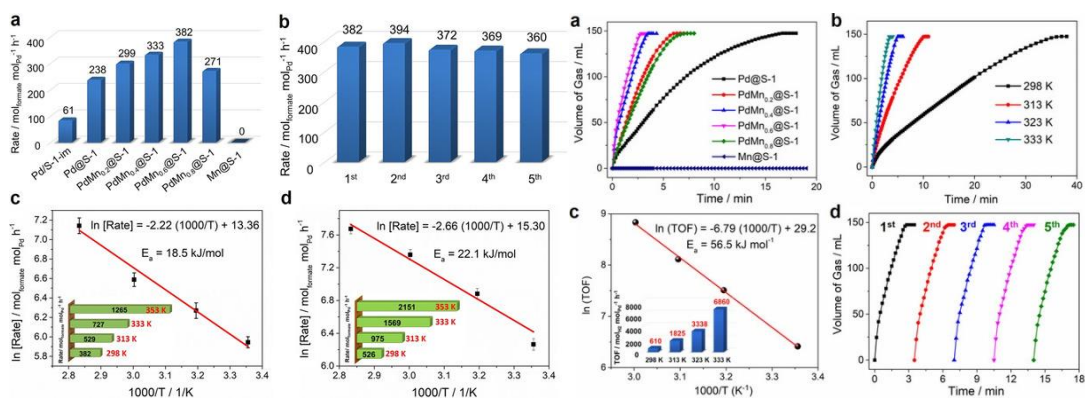
Figure 1.9. *Left (a-d):* (a): CO_2 hydrogenation rates over different catalysts, (b): stability testing of $PdMn_{0.6}@S$-1 catalyst for CO_2 hydrogenation, (c): CO_2 hydrogenation at different temperatures in triethylamine solution over $PdMn_{0.6}@S$-1 catalyst, (d): CO_2 hydrogenation at different temperatures in sodium hydroxide (NaOH) solution over $PdMn_{0.6}@S$-1 catalyst.

Reaction Conditions: catalyst loading (5 mg), solvent (triethylamine or NaOH 1.5 M, 2 mL), and pressure (20 bar, $H_2:CO_2$ 1:1). *Right (a-d):* (a): Formic acid decomposition over different catalysts, (b): Formic acid decomposition at different temperatures over $PdMn_{0.6}@S$-1 catalyst, (c): Arrhenius plot, and (d): stability testing for formic acid decomposition over $PdMn_{0.6}@S$-1 catalyst. Reaction Conditions: catalyst loading ($n_{Pd}/n_{FA} = 0.012$), formic acid (2.0 M, 1.5 mL), and temperature (333 K). Reprinted from the reference [53] with the permission of the Wiley.

Table 1.3. Summary of catalysts investigated for the interconversion reaction between CO_2 and formic acid .

Catalysts	Conditions		TOF (h^{-1})		Stability		Ref.
	H (CO_2:H_2)	DH (FA:SB)	H	DH	H	DH	
Pd/mpg-C_3N_4	(1:2), 150 ºC, 24 h	25 ºC, 180 min	106	144	0	5	[48]
Pd/$CN_{0.25}$	(1:1), 20 ºC, 15 h	25 ºC, 1 h	135,074	5,530	0	6	[49]
PdAg/SBA-15-Amine	(1:1), 100 ºC	(9:1), 75 ºC, 7 h	874	631	0	0	[50]
PdAg/Amine-MSC	(1:1), 100 ºC	(9:1), 60 ºC	839	5,638	3	3	[51]
Pd/AC	30 ºC, 1 h	100 ºC, 40 min	5,504	9,908	5	5	[52]
PdMn$_{0.6}$@S-1 Zeolites	(1:1), 80 ºC	60 ºC, 40 min	2,151	6,860	5	5	[53]

1.6. Catalysis for Bicarbonate – Formate Systems

Cao et al. [54] reported the synthesis of reduced graphene oxide (r-GO) nanosheets supported Pd-based catalysts for the interconversion of potassium-based bicarbonate – formate system to store and release the hydrogen. Using r-GO nanosheets as the supports results in a higher dispersion of metallic Pd nanoparticles, leading to the interconversion reaction even at mild conditions. They reported that careful optimization and control of temperature and hydrogen pressure provide a repetitive cycle of hydrogenation – dehydrogenation using this catalyst without a significant loss of catalyst activity up to 6 cycles.

Lin et al. [44] reported the interconversion of ammonium-based bicarbonate – formate system for the reversible hydrogen storage and delivery using the commercially available Pd-based catalyst supported on carbon, i.e., Pd/C. It has been found that the hydrogen pressure and the temperature are the key controlling parameters for the reaction equilibrium. At room temperature with a hydrogen pressure of 2.75 MPa, 96% yield of ammonium formate via the hydrogenation of ammonium bicarbonate was observed, and nearly 100% hydrogen yield was obtained via the ammonium formate dehydrogenation (**Figure 1.10**).
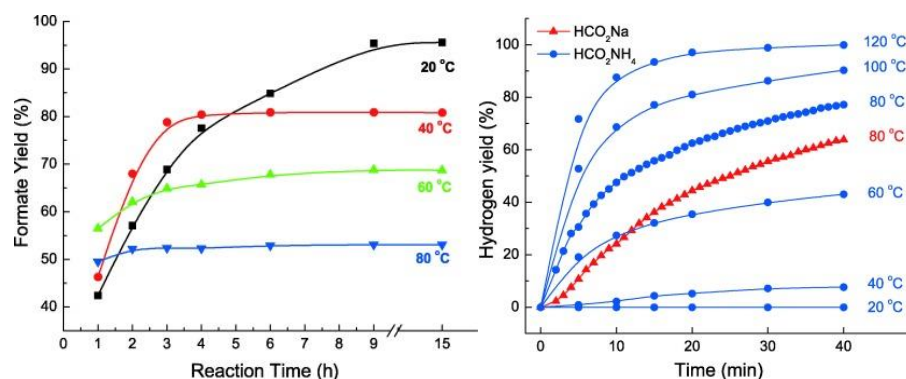
Figure 1.10. *(Left):* Hydrogenation of ammonium bicarbonate and *(Right):* Dehydrogenation of ammonium formate over Pd/C catalyst.

Compared to hydrogenation at lower temperatures and elevated pressure, dehydrogenation was performed at 80 $^{\circ}$C with an initial hydrogen pressure of 0.1 MPa. They found some advantages of heterogenous catalysts over homogenous catalysts. These include the high volumetric density of the hydrogen storage without utilizing any (in)organic additives, easy handling of catalysts, and easy transport of solid hydrogen storage materials, i.e., ammonium formate salt.

Zhang et al. [55], developed the heterogeneous catalysts based on Pd supported on a nitrogen doped carbon nitride support. The aim was to stabilize the Pd nanoparticles on to the support which results in a stable catalyst avoiding the possibility of agglomeration of Pd nanoparticles during the reaction. The results revealed that the developed catalyst showed an excellent performance in the hydrogen storage to the potassium bicarbonate as well as the hydrogen release from potassium formate. It was found that the deposition of Pd nanoparticles over the nitrogen doped support not only stabilize the Pd nanoparticles but also help to tune the electronic structure of the Pd which enables it in hydrogenation as well as in dehydrogenation reactions. In another work [56], they reported the synthesis of Pd-based catalyst where Pd was deposited on the nitrogen doped carbon support. By comparing the effect of support with and without nitrogen support, it was found that the nitrogen functional groups play a significant role in the enhancement of catalyst performance. It could be due to the restraining the Pd nanoparticles agglomeration as well as making the Pd as electron enrich by ligand or electron transfer effect. The electron enriched and well dispersed Pd

nanoparticles behave as an active site for hydrogen activation and atomic hydrogen combining to release the molecular hydrogen in hydrogenation and dehydrogenation, respectively. It was proposed that the nitrogen functionalities might provide the adsorption sites to the positively polarized carbon in the bicarbonate and formate to facilitate the efficient hydrogenation and dehydrogenation, respectively (**Figure 1.11**).

Figure 1.11. Mechanistic view of the bicarbonate – formate hydrogenation – dehydrogenation over the Pd/NMC. Reprinted from the reference [56] with the permission of the Wiley.

Asefa et al. [57], reported the synthesis of Pd-based catalyst supported on the mesoporous carbon where mesoporous carbon support was modified with the polyaniline (PANI) with an aim to incorporate the nitrogen functionalities. The design catalyst revealed an excellent performance in the interconversion reaction of (sodium)bicarbonate – formate system for hydrogen storage and release, respectively. The catalyst composition was optimized by the colloidal silica template and the pyrolysis temperatures which affect the local carbon and nitrogen structure of the nitrogen modified mesoporous carbon supported Pd-based catalysts. It was found that the doping of the nitrogen into the mesoporous carbon support prior depositing the Pd results in the induction of the strong metal-support interactions (SMSI) leading to excellent performance and stability.

Kawanami et al. [58], reported the synthesis of bimetallic catalysts composed of Pd and gold (Au) supported on the phenylenediamine-alkalized (PDA) modified reduced graphene oxide (rGO) support (PdAu/PDA-rGO). The catalyst was subjected to an interconversion reaction for hydrogen storage and release and found that the catalyst was active in both reactions. The excellent performance of bimetallic catalyst was directed to the ligand effect and the strain effect which is caused by the electron transfer effect. Considering the PdAu/PDA-rGO, the oversimplified concept of electronegativity revealed that Pd is electron deficient. A similar study was reported by Shishido et al. [59] on the PdAu/AC catalyst for an interconversion reaction between the (ammonium)bicarbonate – formate system. In both cases, a possible simultaneous electron transfer and strain effect played synergistic role in the active enhancement of the developed catalysts. In another work, Yamashita et al. [60], developed the Pd and silver (Ag) supported on TiO_2 catalysts for the interconversion reaction between (sodium)bicarbonate – formate.

In all above-mentioned bimetallic catalysts, i.e., Ag@Pd@TiO_x/TiO_2 and PdAu/PDA-rGO presents the PdAg and PdAu alloy activity for the hydrogenation of bicarbonate and dehydrogenation of formate. Ag has lower electronegativity, while Au has the highest electronegative metal in the periodic table. However, in both cases, the catalyst revealed improved activity whether the Pd is electron enriched or deficient. The concept of electronegativity is oversimplified. Based on the d-band theory, it can be demonstrated that Pd is electron enriched in both cases.

First, considering the Ag@Pd@TiO_x/TiO_2, the alloy formation of PdAg is followed by the depositing Ag on the surface due to lower surface energies. Therefore, PdAg is mostly preferred from surface alloy or core@shell structures. Interestingly, the d band centers of the Ag relative to

the fermi level were found to be -.94 eV for PdAg alloy. At the same time, pure Ag has a value of -4.12 eV, indicating an upshift in the d band, which implies the flow of electrons from Ag to Pd, leading to the Pd electron enrichment [61]. The electron flow from Ag to Pd makes Ag more affinitive towards the O-species bonding, which is the intermediate in our reaction. The electron enrichment of Pd reduces its coverage from oxygen species, followed by hydrogen dissociation. This phenomenon is also helpful in avoiding Pd catalyst poisoning in a reaction where CO is produced as a by-product. Overall, the d band upshift demonstrates that the activity has improved significantly due to Pd enrichment compared to the monometallic catalyst.

Regarding the potential ligand effects in this catalyst, we may anticipate charge transfer from Pd to Au due to Au higher electronegativity. This statement is correct, yet it is oversimplified. Au typically obtains s and p electrons in bulk PdAu alloys. However, the depletion of Au 5d electrons somewhat compensates for this gain of electrons to Pd. Indeed, it seems that when Au is alloyed, it acquires s, p electrons while losing d electrons, and Pd loses s, p electrons while gaining d electrons. The d-character is much more meaningful than the s, p-character in determining the chemisorption and catalytic capabilities of late-transition metals like Pd and Au. Gaining d electrons in Pd causes the d band center to move away from the Fermi level, reducing interactions between adsorbates and surface Pd atoms. Another factor driving the Pd d band to shrink is a lattice mismatch between Pd and Au, with Pd having a 5% lower lattice constant than Au. In this situation, the length of the Pd-Pd bond increases, raising the Fermi level inside the Pd d band. It also improves the atomic-like property of Pd atoms and, as a result, weakens binding to reactants. We may deduce from both the electron transfer and bond length arguments that Au can lower the binding strength of Pd by perturbing its d band. However, this does not necessarily imply that Au

reduces Pd catalytic activity. As a result, PdAu higher activity is owing to the combined ligand and strain (lattice mismatch) impact [62].

Considering the similar synergistic effects, Shao, and Ji et al. [63], reported the synthesis of Pd supported on the nitrogen and phosphorous co-doped carbon support for the interconversion reaction between the (potassium)bicarbonate – formate system. In their work, with the help of experimental data and density functional theory (DFT) calculations, they found that the electron density enhancement at the Pd results the improved catalyst activity as well as stability. A summary of the catalysts discussed in this section are tabulated in (**Table 1.4**).

1.7. Choice of Metal and Support

It is well known that compared to the carbon supports, the metal-oxide supported catalysts exhibit remarkable properties, including the SMSI and the defects formation with controlled density to stabilize and mobilize the deposited metal nanoparticles and intermediate adsorbed species. Furthermore, the tunable acid-base properties also substantially impact the catalyst's activity under investigation [64]. Compared to metal oxides, including the ZrO_2, CeO_2, ZnO, and MgO, etc., the titania TiO_2 is known to be one of the most investigated catalytic materials and commercialized [65, 66]. Therefore, it is significant to investigate and understand the interactions of the organic species with the TiO_2 supported Pd with and without surface/sub-surface defects in heterogeneous catalysis. It will help us to investigate the mechanistic view of how these specific active sites and defects interact with the intermediate species [67-69]. It is well known that developing next-generation materials on a nano-scale in the past decades allowed us to investigate the two major areas in heterogeneous catalysis.

Table 1.4. Summary of catalysts investigated for the interconversion reaction between bicarbonate and formate.

Catalysts	Cation	Conditions		TOF (h^{-1})		Stability		Ref.
		H	DH	H	DH	H	DH	
Pd/rGO	K	40 bar, 100 °C, 32 h	80 °C, 20 min	7,088	11,299	0	6	[54]
Pd/AC	NH$_4$	28 bar, 20 °C, 15 h	80 °C, 1.5 h	1,769	5,061	5	5	[44]
Pd/NMC	K	60 bar, 80 °C, 2 h	80 °C, 1 h	1,598	2,416	0	0	[55]
Pd/mpg-C$_3$N$_4$	K	60 bar, 80 °C, 1.5 h	60 °C, 5 h	6,595	59%[1]	0	0	[56]
Pd/PDMC	Na	40 bar, 80 °C, 24 h	80 °C, 2 h	1,625	2,562	0	0	[57]
Pd$_{0.5}$Au$_{0.5}$/PDA-rGO	K	50 bar, 50 °C, 16 h	80 °C, 25 min	94%[1]	1,630	0	0	[58]
PdAu/AC	NH$_4$	50 bar, 60 °C	40 °C	5,820	4,200	0	0	[59]
Ag@Pd@TiO$_x$/TiO$_2$	Na	30 bar, 80 °C, 2 h	75 °C, 15 min	820[2]	6,499	0	0	[60]
Pd/N,P-C	K	60 bar, 80 °C, 3 h	80 °C, 130 min	4,269[2]	3,254	0	0	[63]

[1]Yeild and [2]Turnover Number (TON)

First, to establish a clear synthesis-structure-activity relationship and second, to bridge the model studies in surface science and the practical heterogeneous catalysis. Without any doubt, we can say that these two disciplines are necessary and direct the inquiry of others [70-72]. For metal oxide-supported catalysts, considerable work has already been done that link the precision of the catalyst chemistry at the atomic level with the practical applications [73]. Here, we extended such synergistic effects to the hydrogenation of bicarbonate to formate.

Compared to the different noble and transition metals including Au, Ni, and Cu, the Pd has a unique property in that its d-band and Fermi level partially overlaps [74, 75]. The possible reason is that as the Pd has filled the d orbital, i.e., $4d^{10}$, however, the hybridization phenomenon in the solid materials could bring a hole of 0.36 which indicates that Pd even can gain more d electrons from a neighboring metal or support. Such behavior of d electrons of the transition metals determines their adsorption properties compared to their s and p electrons [76]. Based on the classical d-band theory, it has been proposed that the gain of the d electron by shifting d-band of Pd away from the Fermi level leading to the weaker adsorption strength of the adsorbed species over Pd. It could be helpful to avoid Pd poisoning from oxygen species such as carbon monoxide (CO) etc. Additionally, a weaker adsorption strength would enhance the activation of molecular hydrogen on the surface of electron-enriched Pd instead of the strong binding of intermediate species [77].

Commonly, TiO_2 is present in the three structural polymorphs: brookite, rutile, and anatase with less investigated brookite. It could be probably due to synthesis-related and stability issues [78]. However, the rutile is thermodynamically more stable than anatase. Therefore, our study employed anatase due to the following facts. Additionally, the anatase (101) has a surface energy

26

(0.44 J/m^2) lower than rutile (0.9 J/m^2), which makes it easy to synthesize without any capping agents and stabilize the deposited metal nanoparticles [79]. The excellent charge transfer properties and lower band gap of the TiO$_2$ could be directed to the narrow electronic levels stimulated by the oxygen vacancies. It was proposed that the oxygen defects behave as a local factor that interacts with the deposited metal nanoparticles and adsorbed species and favors efficient charge transfer. The defect state of TiO$_2$ (Ti 3d) in the bandgap of TiO$_2$ directed to the Ti interstitials resulted in the narrow bandgap [80]. Furthermore, theoretical calculations revealed that the oxygen vacancy formation energies are lower for the anatase than the rutile [80].

Goren et al. [81] reported the hydrogenation of bicarbonate to formate over the Pd/TiO$_2$. Their early work, i.e., 3 decades ago, demonstrated that the metallic Pd is the active site for the dissociation of molecular hydrogen and the adsorption of bicarbonate species. They claimed that the charge transfer from TiO$_2$ to Pd favors bicarbonate hydrogenation. Mori et al. [82] reported a Pd bimetallic catalysts (Cu, Zn, Au, and Ni as 2nd metal) supported on different supports including the TiO$_2$, CeO$_2$, Al$_2$O$_3$, MgO, and LDH for bicarbonate hydrogenation to formate. They found that the PdAg/TiO$_2$ is the most active catalyst. Additionally, together with DFT calculations and experimental findings, they proposed that there is an electron transfer from Ag to Pd, probably due to the higher electronegativity of Pd than Ag, making it more electron enriched. The Pd was proposed to be an active site for hydrogen activation while electron deficient Ag was assumed to be the active site for the adsorption of intermediate species. Masuda et al. [60] reported the Ag@Pd/TiO$_2$ catalyst for the bicarbonate-formate system. They proposed that the Pd-TiO$_2$ interface is the active site for the hydrogenation of bicarbonate to formate where Pd was found to be electron enriched due to the electron transfer from both Ag and TiO$_2$.

1.8. Challenges and Research Objectives

Based on the literature mentioned above, it has been found that the development of a catalyst with high activity in hydrogenation and dehydrogenation while maintaining long-term stability is still under development. The most common issue with catalyst deactivation is agglomeration, probably due to weak metal-support interactions because of a wider band gap and poor electron mobility. We aim to synthesize and characterize the palladium (Pd) supported by titania (TiO_2) with controlled oxygen vacancies. It hypothesized that the bridged oxygen vacancies would provide anchoring sites to Pd with good electron mobility from support to metal due to a narrow band gap. As a result, strong metal-support interactions (SMSI) will exist, eliminating the possibility of agglomeration and making the catalyst active and stable because of the tuned adsorption properties of intermediates and hydrogen (reverse)spillover.

CHAPTER 2: METHODOLOGY

2.1. Chemicals and Gases

All the chemicals employed in this research were acquired by the Sigma – Aldrich with maximum purity and used without any further purification .

2.2. Synthesis of Mesoporous Titania

A modified approach was used to prepare the mesoporous TiO_2 nanoparticles via the Sol-Gel method [83]. In a typical synthesis, the surfactant, Pluronic F-123 (5 g), was initially dissolved into the ethanol (30 mL) and hydrochloric acid (HCl, 0.8M) diluted in deionized water (DI). The solution is stirred for 4 hours to favor surfactant organization into micelles by forming a clear solution. After that, another solution was prepared by mixing the titanium isopropoxide (14.2 g) into ethanol (30 mL). The first clear solution was added to the titanium isopropoxide and stirred until the formation of the gel. The gel was kept under the aging process at 50 ^{o}C for 16 hours. After that, the gel was dried at 50 ^{o}C, followed by washing with ethanol twice and drying at 125 ^{o}C for 5 hours. Removal of surfactant was carried out by calcinating the $mTiO_2$ at a temperature of 450 ^{o}C for 2 hours (5 ^{o}C/min).

2.3. Pre-Reduction of Mesoporous Titania

As-synthesized $mTiO_2$ was subjected to the pre-reduction process via a reported method [84]. In a typical method, as-synthesized $mTiO_2$ was placed in a tube furnace and reduced under pure H_2 flow (80 mL/min) at different temperature between 300 ^{o}C and 700 ^{o}C. for 3 h with a heating rate of 10 ^{o}C/min. The collected reduced black powder was labeled as TiO_{2-x} – 300 ^{o}C, TiO_{2-x} – 300 ^{o}C, TiO_{2-x} – 300 ^{o}C, TiO_{2-x} – 300 ^{o}C, and TiO_{2-x} – 300 ^{o}C.

2.4. Synthesis of TiO₂ Supported Pd Nanoparticles-based Catalysts

In a typical procedure, support TiO_{2-x} (500 mg) was suspended into the acetone solvent (40 mL). A known amount of Pd precursor, i.e., palladium acetate for a Pd loading 3 wt.% was separately dissolved into the acetone solvent (40 mL). The later solution was mixed into the first one and subjected to rigorous stirring until the complete vaporization of the acetone solvent. The dried samples were poured into deionized water (40 mL) and stirred continuously. Sodium borohydride with a molar ratio approximately 10 times than the Pd was added dropwise to reduce the Pd into metallic state. After adding sodium borohydride, the solution was further stirred for another 1 hour. Finally, the solid product was filtered out after successive washing with acetone and deionized water followed by overnight freeze drying to get $Pd3/TiO_{2-x}$.

2.5. Characterizations

A scanning electron microscopy (SEM Quanta) was used to acquire the images of the samples to look into morphology. The specific surface area of the mesoporous titania was estimated by using the Brunauer-Emmett-Teller (BET) method. The Bruker D8 Advanced diffractometer was employed for the powder X-ray diffraction (XRD) analysis under operating conditions of 40 mA and 40 kV for CuKα ($\lambda = 0.15406$ nm), with a scan range of 5-90° at an operating speed of 4 ° min⁻¹. H_2-TPD, H_2-TPR, and O_2-TPD were performed to investigate the hydrogen interactions with the supported metal nanoparticles, catalyst reducibility, and oxygen vacancies, respectively. In a typical procedure, a known amount of catalyst (200 mg) was loaded in a quartz tube and subjected to pretreatment under Argon at a temperature of 300 °C, 50 °C/mins, with hold time of 10 minutes. After that sample was treated and saturated under respective gas based on the analysis for 60 minutes. Carrier gas was purged to remove the weakly adsorbed species. The temperature was raised to 900 °C, 10 °C/mins, with hold time of 30 minutes to record the TCD signal versus

temperature and time. NH$_3$-TPD was performed to probe the acidic sites on the catalyst surface. Typically, a sample with a known amount, i.e., 100 mg, will be pre-treated in an inert gas for 1 hour at 300 ^{o}C. Afterward, NH$_3$ balanced with He will be flowed to saturate the sample at 50 ^{o}C. Then, the sample will be fluxed with a helium stream for 15 mins to remove the excess NH$_3$ before increasing the temperature to 900 ^{o}C at a heating rate of 10 ^{o}C/min. NH$_3$ desorption will be scanned by a thermal conductivity detector (TCD) and a mass spectrometer (MS). Oxygen pulse chemisorption was used to quantify the amount of surface oxygen vacancies on catalyst. The surface functional groups analysis and to probe the reaction mechanism, the FTIR and in-situ ATR-FTIR analysis were performed by using the Bruker Tensor II spectrometer equipped with the Harrick Horizon (ZnSe) and a Harrick temperature control system (ATC-024-4). Liquid samples collected from hydrogenation reaction were filtered through a 0.22 µm pore-size filter for analysis in the high-performance liquid chromatography (HPLC) equipped with a dual UV-VIS Detector (Shimadzu SPD 10-AV) at 208 and 290 nm and a Refractive Index Detector (Shimadzu RID-10A). for the analysis of samples, the samples were subjected to separation in a Bio-Rad (4 Aminex 87-H) column using mobile phase composed of sulfuric acid (5 mM) at a flow rate of 0.7 mL/min and a column temperature of 55 ^{o}C. The X-ray photoelectron spectroscopy (XPS) measurements were carried out using a Thermo-Fisher NEXSA spectrometer with full 180° hemispherical analyzer, mean radius (125 mm), and channel detector (128).

2.6. Catalyst Experimental Evaluation

In a typical hydrogenation experiment, a known amount of catalyst was loaded into the reactor (Series 4590 Micro Stirred Parr Reactors, 100 mL) with ammonium bicarbonate (1M, 30 mL). It was followed by purging with nitrogen (N$_2$) 3 times and H$_2$ charging at 500 psi for desired reaction time. After the reaction, the H$_2$ was released, and the sample was filtered out to collect

the liquid sample for analysis in HPLC. In a typical dehydrogenation experiment, a known amount of catalyst was dispersed into 10 mL of DI water and charged into the reactor. The reactor was subjected to heating up to 80 °C after purging it with nitrogen (N_2) 3-times. Once the desired temperature was reached, 10 mL of ammonium formate (2M) was injected to make the overall concentration and volume into the reactor 1M and 20 mL, respectively. The generation of H_2 was monitored and recorded through a calibrated H_2 flowmeter for 40 minutes each run. A CO_2 trap composed of sodium hydroxide (NaOH, 7M, 120 mL) was used to trap the CO_2 produced by the ammonium bicarbonate's thermal decomposition.

2.7. Density Functional Theory (DFT)

Energy and charge density analysis calculations were performed using Density Functional Theory (DFT) in the projector-augmented wave formalism [85, 86] using the code VASP [87-90]. The plane wave basis set energy cutoff of 400 eV was used, and Gaussian smearing was used with a smearing width of 0.05 eV. Since relatively large simulation cells were adopted, only the gamma point was used to sample the Brillouin zone. Spin-polarized DFT calculations were performed for all geometry relaxations. Geometries were optimized with a force convergence criterion of 0.02 eV/A, and total energies converged to at least 10^{-6} eV. The RPBE functional [40] was employed with Grimme's zero damping DFT-D3 method [41,42] for van der Waals (vdW) corrections. The DFT+U method [91] within VASP has been used for Ti d states with a $U_{eff} = 3$ eV to correct for on-site coulombic interaction, as suggested by Hu and Metiu [92].

The Pd/TiO_2 catalyst interface with oxygen-based support modifications was constructed using a 55-atom Pd cluster and a single-layered anatase TiO_2 (101). The unit cell, sized approximately 30.26×33.00 Å consisting of 343 atoms, was constructed, and optimized using

32

DFT. The Pd3/TiO_2 catalyst interface (Pd3/TiO_2 – 500 ºC) with O vacancies was constructed by pulling away the nearest 12 oxygen atoms around the Pd cluster over the TiO_2 surface. Dipole corrections were applied in the surface-normal direction to all periodic surface slabs. Bader charge analysis was performed to quantify the corresponding surfaces' charge transfer across the interface.

CHAPTER 3: RESULTS AND DISCUSSIONS

3.1. Synthesis of Support and Catalysts

Mesoporous TiO_2 ($mTiO_2$) was synthesized via the sol-gel method to cope with the lower specific surface area (SSA) of commercial TiO_2 ($cTiO_2$) and metal sintering [29]. Pluronic P-123, a non-ionic block polymer, was used as a directing agent with optimized solvent, hydrolysis ratios, titanium precursor, and surfactant concentration. Scanning electron microscopy (SEM) images are provided in (**Figure 3.1**) which indicates a wide particle size distribution (PSD). The Brunauer, Emmett and Teller (BET) analysis (**Figure 3.2**) resulted in an adsorption-desorption isotherm of Type IV, indicating an mesoporous structure. The SSA is found to be 116.64 m^2/g, while the Langmuir surface area of 253.09 m^2/g. The average pore diameter is 4.3185 nm which falls within the range of mesoporous pore size. For the synthesis of TiO_2, the surfactant-facilitated routes were preferred as they provide various interactions such as covalent bonding, hydrogen bonding, and electrostatic and van der Waals interactions. It was found that an interaction balance results in the achievement of self-assembly, leading to a range of textural characteristics and structural orders. Compared to ionic, non-ionic surfactant was used in this work which provides a medium interaction with the titania walls leading to easy removal. It has been found that the inorganic surfactants facilitate the metal oxide-surfactant composites formation based on the inorganic framework organization via hydrogen bonding.

The hydrolysis molar ratio is one of the key parameters in synthesizing mesoporous TiO_2. The water encourages the TiO_2 synthesis by facilitating the hydrolysis and condensation reaction of Ti precursor, influencing the interaction types, and enhancing the reaction medium polarity for the more ordered self-organization of surfactants into micelles [93-95]. In our case, the hydrolysis progress and condensation reaction is evaluated by the solvent type and nature, i.e., ethanol. The

solvent is responsible for providing the hydroxyl groups together with the determination of the structure of the final metal oxide [96-98]. Under the synthesis conditions, the solvent facilitates the trans-alcoholysis reaction between the isopropoxide groups and the solvents [93, 94]. It has been found that the micelles organization occurs when the critical micelles concentration (CMC) is reached; therefore, optimizing the surfactant concentration ratio is essential [99-101]. The rate of the hydrolysis and condensation reaction is ultimately related to the choice of the Ti precursor, titanium isopropoxide, in our case. Inorganic sources such as $TiCl_4$ are found to be unfeasible due to their high reactivity and difficulty handling. Besides, titanium alkoxides were more effective because of their high safety and chemical stability. Furthermore, the alkoxyl groups behave as controllers in the reactions due to the steric inhibitions providing sufficient time between the surfactant and TiO_2 to develop the interactions [102, 103].
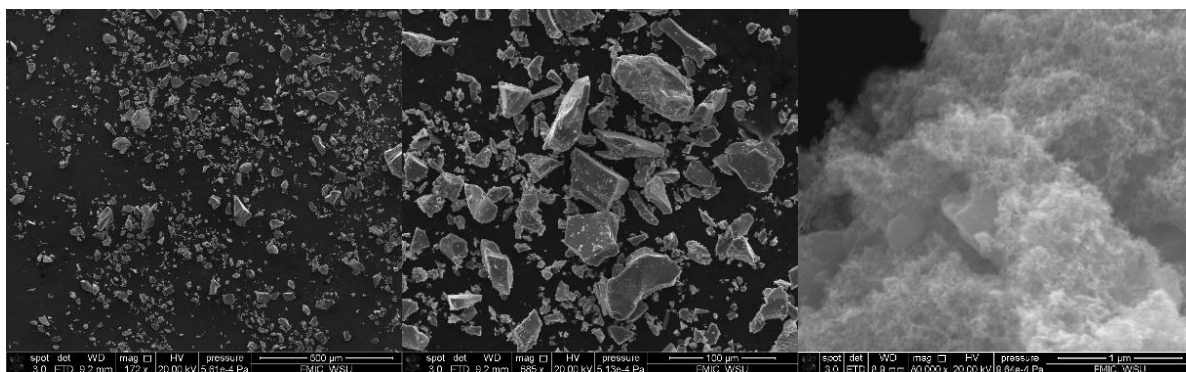
Figure 3.1. SEM images of the mesoporous TiO_2 support synthesized by using titanium isopropoxide as precursor via Sol-Gel method.
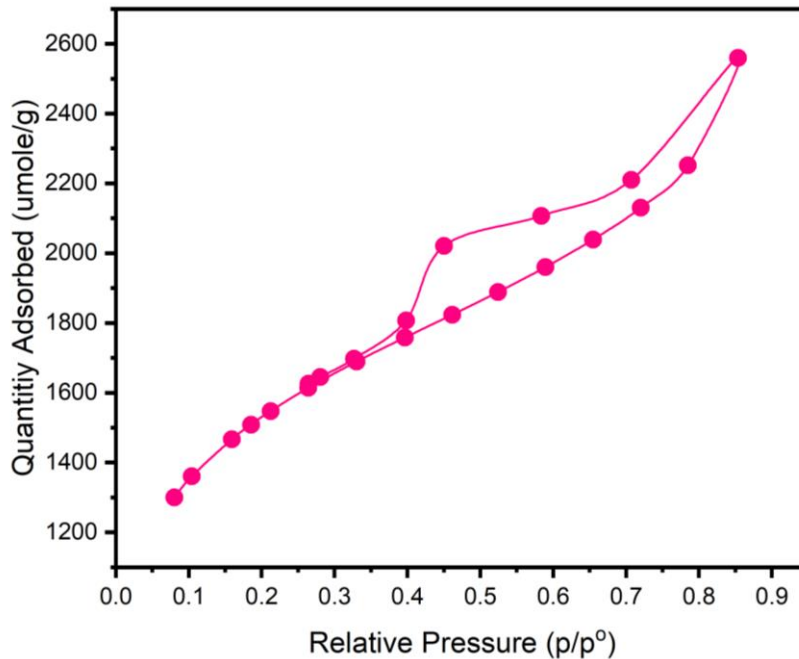
Figure 3.2. Nitrogen (N_2) adsorption-desorption isotherm indication the mesoporous structure of synthesized mesoporous TiO_2.

From the FT-IR spectra (**Figure 3.3**), broad peaks appeared in the as-synthesized TiO_2 (TiO_2 – AS) sample around ~2920 cm^{-1} and ~2854 cm^{-1} and other spectra near ~1520 cm^{-1} and ~1720 cm^{-1}. These spectra indicate the existence of the symmetric -CH and asymmetric -CH_2 vibrational modes of the organic solvent (ethanol) and the Ti template together with TiO_2, respectively. Both these spectra mentioned above disappeared completely upon calcination at elevated temperature, i.e., 500 °C in the calcined sample (TiO_2 – C) as well as in the reduced sample (TiO_2 – R) [104]. The strong band that appeared in the range of 900-400 cm^{-1} indicates the vibrational modes of the Ti-O in TiO_2 [105]. Another broad range of peaks appeared between 3800-300 cm^{-1}, indicating the presence of stretching vibrational modes of -OH from the physically adsorbed water molecules [106].
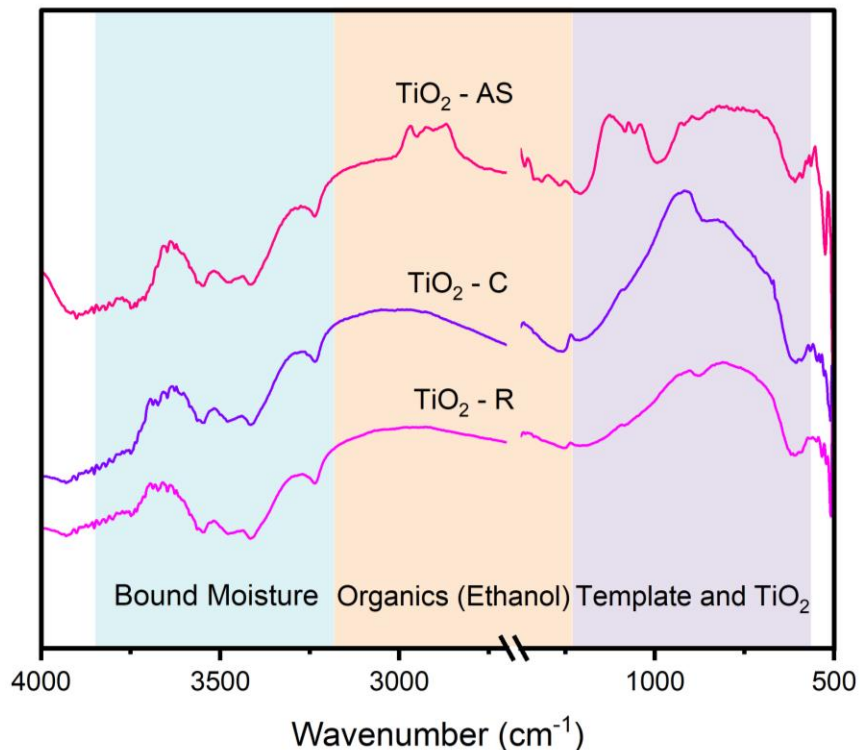
Figure 3.3. FT-IR spectra of as-synthesized, calcined, and reduced mesoporous TiO_2.

3.2. Catalyst Synthesis, Morphology, and Structure

The diffractograms of the different supports and catalysts (**Figure 3.4**) do not show any evidence of either the rutile or brookite phase of TiO_2. Instead of rutile or brookite, the diffractograms revealed the TiO_2 with anatase as dominant phase. The different peaks for the anatase phase are located at 25.15º, 37.82º, 47.98º, 53.88º, 55.01º, 62.73º, 68.73º, 70.32º, and 74.92º corresponding to the (101), (001), (100), (105), (211), (102), (116), (220), and (215) lattice planes, respectively [107]. In the bulk anatase phase of TiO_2, the coordinatively unsaturated Ti_{5C} and O_{2C} behave as a Lewis acidic and basic center with both (101) and (001) facets. These Lewis acidic and basic center (acid-base pairs) could facilitate the hydrogenation reactions (**Figure 3.5**). The anatase supposed to be exhibit lower surface energy of 0.44 J/m^2 than rutile, which has 0.99

37

J/m^2. However, their activities trend could differ depending on the reactions and active site requirements. Furthermore, the anatase exhibits both Lewis acid and Bronsted sites while rutile only possesses Lewis's acid sites [107-109]. The possible existence of Bronsted sites, i.e., hydroxyl (OH) groups on anatase, could help the efficient hydrogenation and will be discussed in detail in succeeding sections.
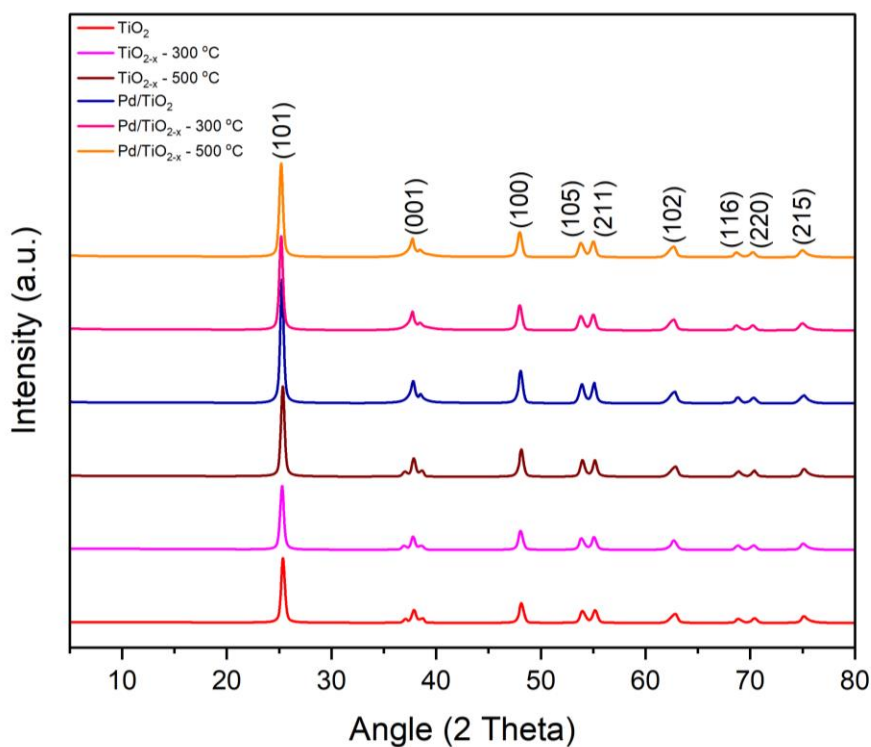
Figure 3.4. XRD analysis of catalysts and supports.
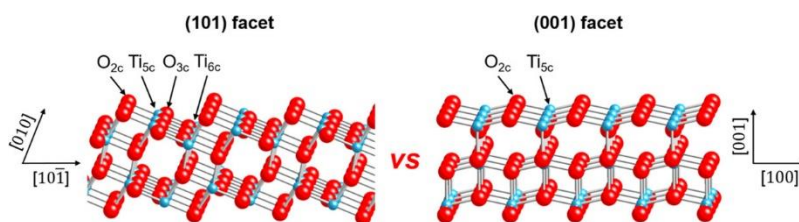
Figure 3.5. Models of TiO$_2$ with anatase (101) and rutile (001) dominated facets.

3.3. Catalyst Composition

XPS analysis was performed to investigate the oxidation states of the elements in the catalysts. (**Figure 3.6**) represents the XPS spectra of Pd 3d, with two prominent peaks around 334.33 eV and 339.59 eV that can be assigned to the Pd^0 $3d_{5/2}$ and Pd^0 $3d_{3/2}$ spin-orbital spitting, respectively. The other two peaks, around 336.16 eV and 341.32 eV, indicate Pd partial oxidation state, i.e., PdO $3d_{5/2}$ and PdO $3d_{3/2}$ spin-orbital spitting, respectively. From these peaks, it can be said that the metallic Pd dominates in the samples and behaves as an active center for the hydrogenation reaction. (**Figure 3.7**) represents the XPS spectra of Ti 2p, which can be divided into three distinguished peaks at 458.5 eV, 464.2 eV, and 460.4 eV, which can be assigned to the Ti^{+4} $2p_{3/2}$, Ti^{+4} $2p_{1/2}$, and Ti^{+3} $2p_{3/2}$, respectively. The peak Ti^{+3} $2p_{3/2}$ can be directed to the oxygen vacancy-induced state of Ti. In all catalysts, Ti^{+3} oxidation state can be observed to various extents depending on the concentration of oxygen vacancies [110]. (**Figure 3.8**) represents the XPS spectra of O 1s with three peaks which can be directed to the lattice oxygen (529.46 eV), oxygen vacancy (531.15 eV), and chemisorbed oxygen (542.35 eV). The oxygen vacancy peak is expected to be within the range of 1-2 eV of the lattice oxygen peak. However, O 1s is not an authentic way to explore and quantify the oxygen vacancies for many reasons. One of the possible reasons may be the existence of oxygen vacancies on the surface and in the sub-surface. Still, XPS may be unable to identify all the sub-surface oxygen vacancies. The second and more practical reason is the oxygen vacancy band energy overlapping with other species. It is admitted that the oxygen vacancies can be healed upon exposure to a higher concentration of oxygen species, such as air or moisture, with much weaker bonding compared to the lattice bond. The O 1s peak assigned to the oxygen vacancies may be overlapped with the absorbed hydroxyl groups on the metal originating from the environmental moisture. It could be due to the O_2^{-2} species [110, 111].
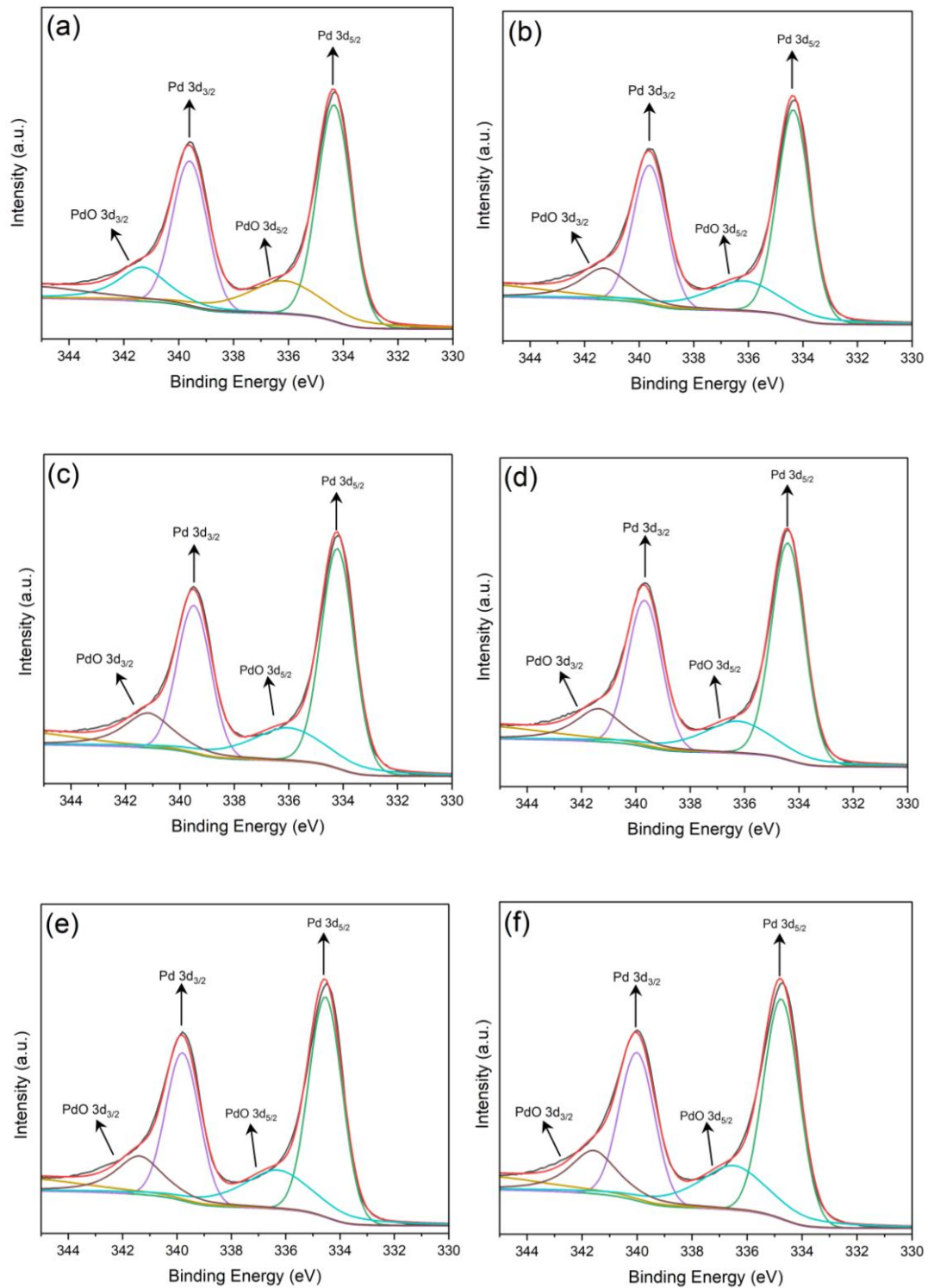
Figure 3.6. Pd 3d XPS spectra of (a): Pd3TiO$_2$, (b): Pd3TiO$_{2-x}$ – 300 ^{o}C, (c): Pd3TiO$_{2-x}$ – 400 ^{o}C, (d): Pd3TiO$_{2-x}$ – 500 ^{o}C, (e): Pd3TiO$_{2-x}$ – 600 ^{o}C, and (f): Pd3TiO$_{2-x}$ – 700 ^{o}C.
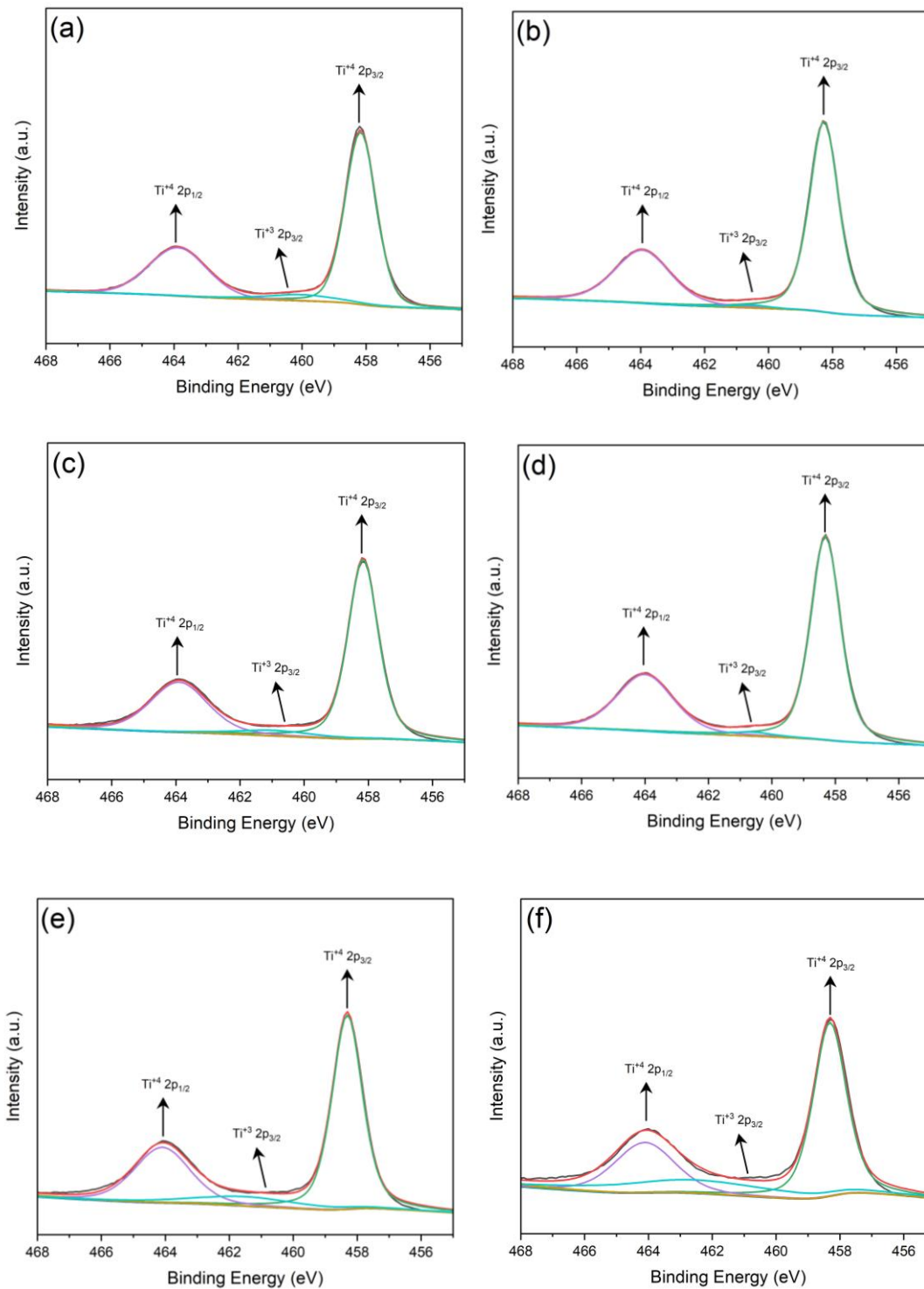
Figure 3.7. Ti 2p XPS spectra of (a): Pd3TiO$_2$, (b): Pd3TiO$_{2-x}$ – 300 ^{o}C, (c): Pd3TiO$_{2-x}$ – 400 ^{o}C, (d): Pd3TiO$_{2-x}$ – 500 ^{o}C, (e): Pd3TiO$_{2-x}$ – 600 ^{o}C, and (f): Pd3TiO$_{2-x}$ – 700 ^{o}C.
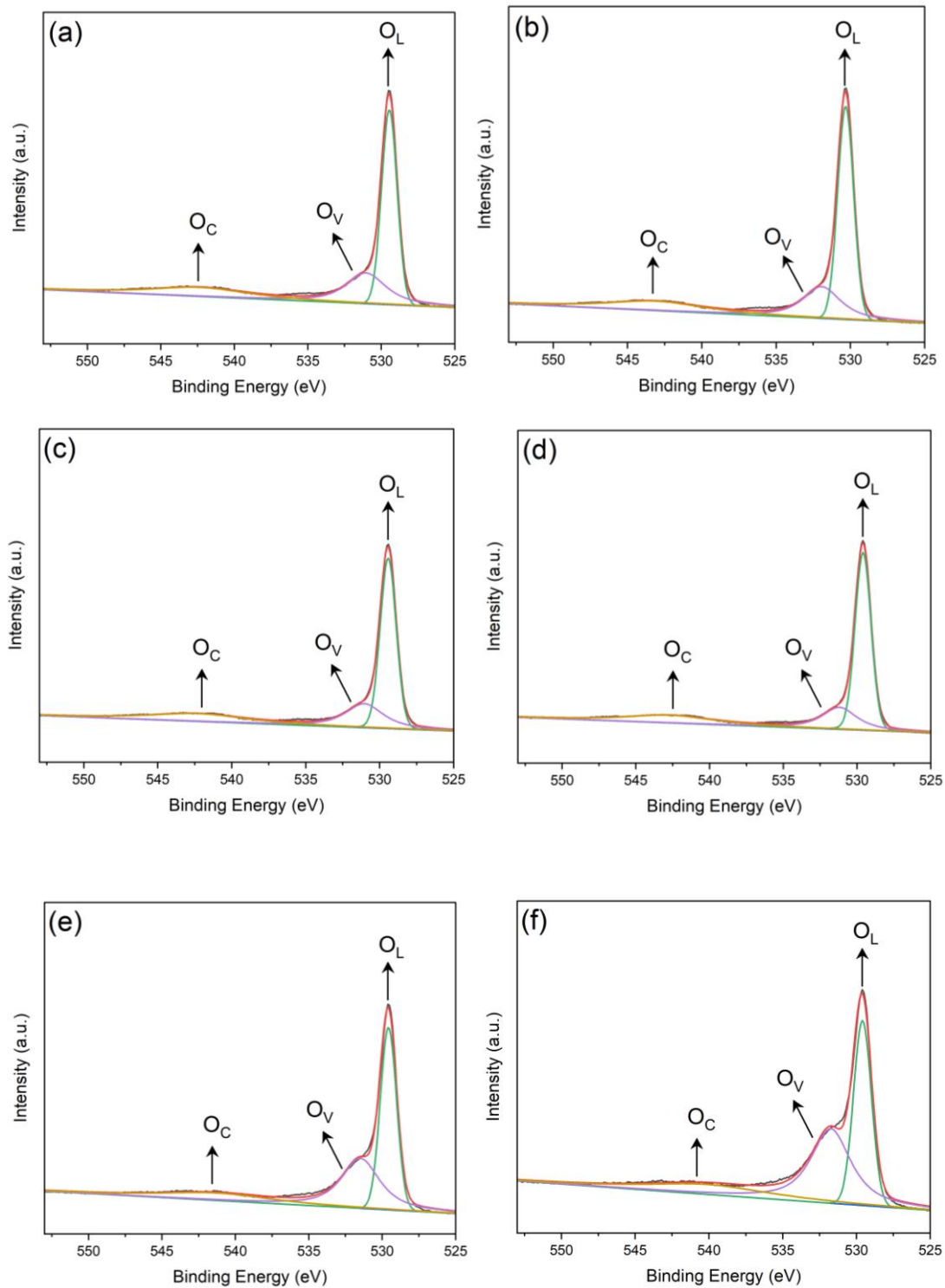
Figure 3.8. O 1s XPS spectra of (a): Pd3TiO$_2$, (b): Pd3TiO$_{2-x}$ – 300 ^{o}C, (c): Pd3TiO$_{2-x}$ – 400 ^{o}C, (d): Pd3TiO$_{2-x}$ – 500 ^{o}C, (e): Pd3TiO$_{2-x}$ – 600 ^{o}C, and (f): Pd3TiO$_{2-x}$ – 700 ^{o}C.

3.4. Catalyst Reducibility, H₂ Activation, and O₂ Mobilization

To investigate the reducibility and the hydrogen spillover behavior of the catalysts with surface active oxygen species, the H_2 TPR analysis has been performed (**Figure 3.9**). Overall, three peaks were exhibited by all catalysts. The sharp negative peak at low temperatures indicates the decomposition of Pd β-hydride which takes place immediately after hydrogen and Pd interact with each other at the beginning of the TPR analysis. Higher intensity of negative peak indicates the higher H_2 activation due to Pd electron enrichment [112, 113]. The first low-temperature small peak in a region <400 °C suggests the reduction of surface PdO_x species. It could also the reduction of the surface active TiO_2-based oxygen species around the Pd species due to the H_2 spillover effect [114-117]. The high-temperature peaks, i.e., >400 °C, indicate the reduction of sub-surface PdO_x species and the surface active oxygen species of TiO_2, which are away from the Pd nanoparticles. From the results, it can be seen that with an increase in the oxygen storage capacity, i.e., oxygen vacancies, the intensity of the high-temperature peaks, i.e., >400 °C, reduced, indicating the higher ratio of Pd/PdO_x as well as the H_2 spillover effect. The H_2 spillover effect facilitates the reduction of supported catalysts. A similar trend was observed in terms of the peak temperature shifting. It indicates that as oxygen storage capacity, i.e., oxygen vacancies, increases, the temperature makes a lower shift indicating the formation of larger Pd nanoparticles with electron enrichment. The larger Pd nanoparticles are easy to reduce, and their electron enrichment will facilitate the H_2 activation during hydrogenation [118].
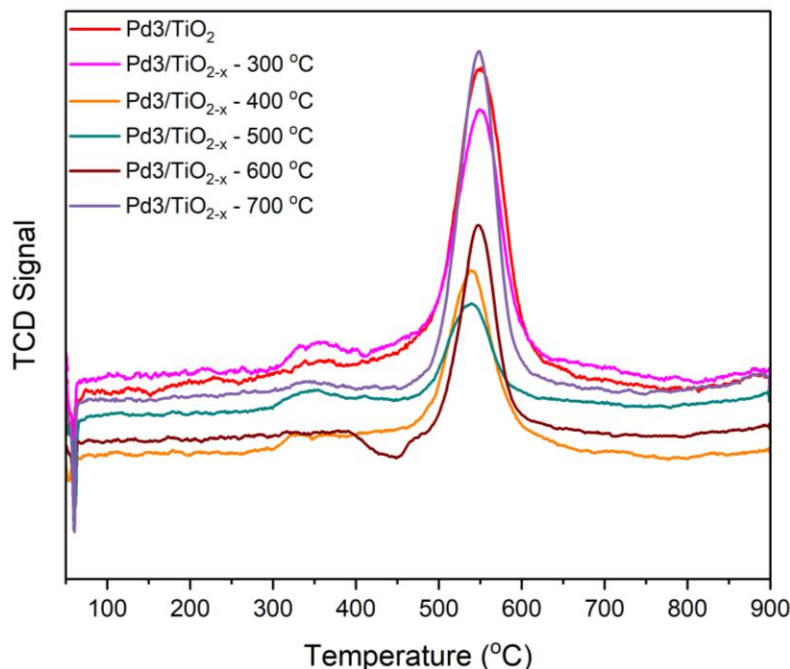
Figure 3.9. H_2 – TPR analysis of catalysts with varying level of oxygen vacancies.

To investigate the activation of molecular hydrogen, i.e., heterolytic dissociation at the metal surface and spillover towards the support due to concentration gradient can be identified by using a combination of H_2-TPD and in-situ DRIFTS experimentation. The H_2-TPD analysis has been performed for the catalysts, and the results are shown in (**Figure 3.10**). The regions of H_2-TPD can be divided into four regions. These regions include within the temperature range of <150 °C, <275 °C, 400 °C, and 610 °C. The region <150 °C represents the reversible desorption of hydrogen, while the other three regions indicate the irreversible desorption of hydrogen [119]. (**Figure 3.10**) indicate the existence of irreversible hydrogen desorption from the metal nanoparticle, metal-support interface, and support. Furthermore, a broad peak centered at 180 °C indicates the hydrogen desorption from the metal nanoparticle. The shoulder peak, centered at 430 °C and 550 °C, shows the hydrogen desorption from the metal support interface and support, respectively, facilitated by the hydrogen spillover (Figure 9c) [114]. Less hydrogen desorption in

the Pd3/TiO$_{2-x}$ – 500 $^{\circ}$C catalyst from the sub-surface of support indicates that the sub-surface

oxygen vacancies are stable in anatase and accommodate hydrogen favorably. This effect could

be helpful in the technological applications of hydrogen storage materials [120]. The TiO$_2$ with

dominant (101) facets is supposed to have approximately 40% higher storage capacity than the

(001) facet, as identified in XRD.
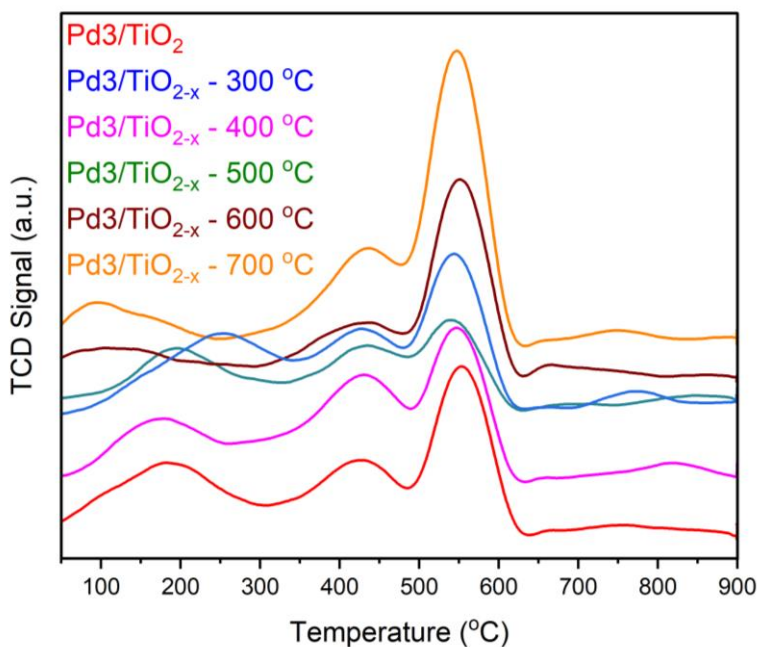
Figure 3.10. H$_2$ – TPD spectra of catalysts.

One of the aims behind creating oxygen vacancies was to mobilize and stabilize oxygen

species, intermediate (HCO$_3^{-1}$). For this purpose, the O$_2$ TPD analysis was carried out (**Figure

3.11**). From the results, the surface coverage/desorption of O$_2$ reduced with an increase in the

oxygen vacancies. Additionally, the desorption peak indicates the O$_2$ desorption from the sub-

surface. In anatase (101), the Ti$_{5C}$ – O$_{2C}$ bond stiffness results in the oxygen vacancies localization

in the sub-surface or bulk [121-124]. Concerning the O$_2$ interaction with the Ti interstitials and

45

oxygen vacancies, it has been noticed that the defects are not negative charge source only. Defects actively react with the O_2, although localized in the sub-surface. It can be argued that the adsorption of molecular O_2 facilitates the defect's migration from the sub-surface to surface. Ti interstitials can form a TiO_2-like island by reacting exothermically, and oxygen vacancies accommodate the O_2 molecules. It might be why an increase in defects results in lower O_2 desorption. Hence, both defects facilitate the energetically O_2 incorporation into the anatase TiO_2.

Together with H_2-TPR and H_2-TPD, we can conclude that the oxygen vacancies have been formed successfully by removing the (sub)surface active oxygen at different temperatures using H_2. In addition, the evidence of H_2 spillover also indicates that the catalyst can perform better than the reported catalyst at room temperature with high activity and stability. The O_2-TPD provides a signal of stabilization of oxygen species, mainly intermediate species or PdO, during the catalyst synthesis.
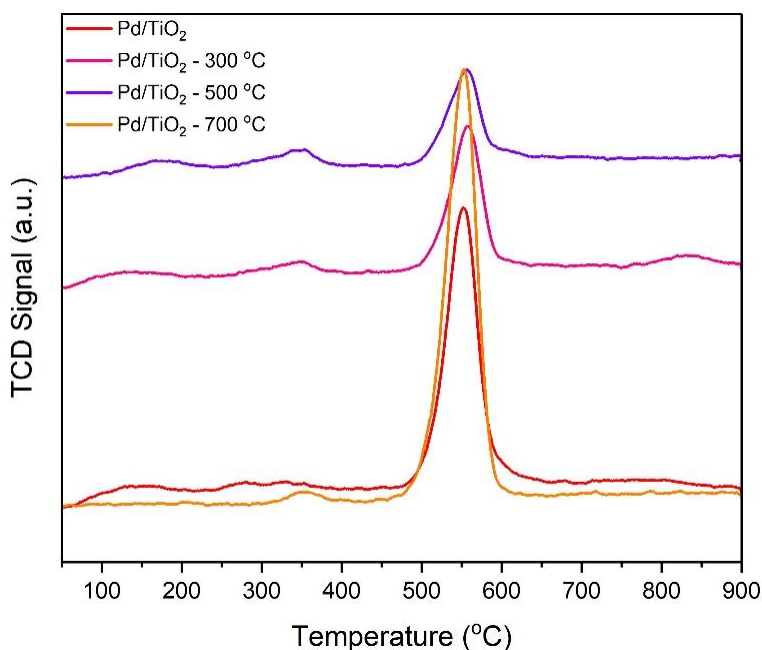
Figure 3.11. O_2 – TPD spectra of catalysts with different concentrations of oxygen vacancies.

3.5. Nature and Strength of Active Sites

As the intermediate species, i.e., bicarbonate is a weak base in nature, it is important to investigate the acidity of the support which can facilitates the adsorption of intermediate to the support. For this purpose, NH_3 – TPD analysis has been performed and results are provided in (**Figure 3.12**). In case of Pd/TiO_2, one major peak appeared between 100-150 ^oC which can be directed to the weak acidic sites due to the less oxygen storage capacity/oxygen vacancies. When the concentration of oxygen vacancies is increased to Pd/TiO_{2-x} – 300 ^oC and Pd/TiO_{2-x} – 500 ^oC, the intensity of the peak reduced with a slight shift to higher temperature and finally appearance of a medium acidic site peak around 400 ^oC. It indicates that an increase in the oxygen vacancies results in the acidic sites from weak to medium. To gain insight into the NH_3 – TPD, it is essential to know the electronic nature of oxygen vacancy. It is well admitted that forming the oxygen vacancies in the transition metal oxides, i.e., TiO_2, is a complex solid-state redox process.
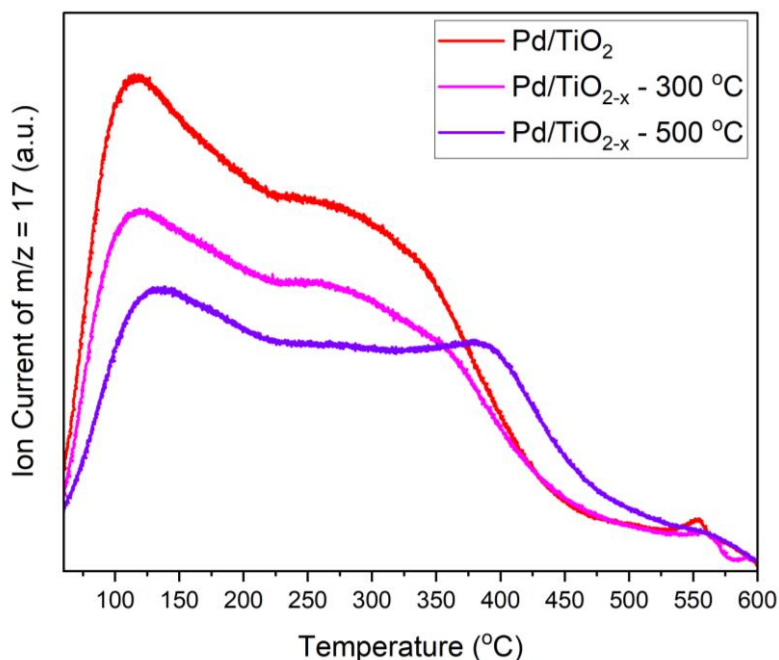
Figure 3.12. NH_3 – TPD spectra of catalysts with different oxygen vacancy concentrations.

It involves the exchange of oxygen into or from the surroundings leading to the transfer of electronic charge into or from the material [125, 126]. By removing the oxygen, the two electrons which were formerly bounded to the oxygen ion remains in the TiO_2 with an increase in the local charge density [127]. Hence, the energy level of the oxygen vacancy can behave as an electron-donor state or as an acidic site. These sites play a critical role in the adsorption of oxygen species such as bicarbonates [128, 129].

3.6. Identification of H_2 Spillover in Liquid Phase Reactions

Due to the presence of a solvent, H_2 spillover becomes more complicated to identify compared to the gas phase reactions. The typical way to identify H_2 spillover in a liquid phase reaction is based on the same characterization techniques employed in the gas phase with slight modifications. To identify the H_2 spillover in the liquid phase, it is necessary to go back to the origin of the concept of the H_2 spillover. One of the most common ways is to monitor the color changes of the tungsten oxide (WO_3) during reduction [130]. It is well known that the (**Figure 3.13**).

Initially, DI water (30 mL) was taken, and 1 gram of tungsten oxide was mixed in a reactor. The system was charged with H_2 gas at a pressure of 500 psi and at room temperature for 1 hour. After 1 hour, the reactor was opened, and no significant change in tungsten oxide color was found. It indicates that the reduction might be prolonged as there was no spillover of H_2, as the metal to activate the H_2 was missing. After that, 50 mg of $Pd3/TiO_{2-x}$ – 500 °C was added to the mixture and the identical experiment was repeated. After 1 hour, it was found that the reaction mixture had turned a dark blue color. The color change indicates that the molecular hydrogen was dissociated at the Pd and spilled to the tungsten oxide to reduce it quickly [130].

Figure 3.13. Evidence of H_2 spillover in liquid phase reactions. From *left to right*, (1): WO_3 + H_2O, (2): WO_3 + H_2O + H_2, (3): WO_3 + H_2O + Catalyst, and (4): WO_3 + H_2O + Catalyst + H_2. Catalyst: Pd3/TiO$_{2-x}$ – 500 ºC.

3.7. Oxygen Storage Capacity and Catalyst Activity

To investigate the relationship between activity and oxygen vacancies, catalysts were evaluated for the hydrogenation of ammonium bicarbonate. The results are provided in (**Figure 3.14**). The oxygen vacancies were quantified using the oxygen pulse chemisorption to calculate the oxygen storage capacity (OSC). Both the rate and the OSC exhibited a volcano chart by revealing that the catalyst Pd3/TiO$_{2-x}$ – 500 ºC shows the highest amount of OSC with a higher activity. The role of oxygen vacancies in enhancing activity can be elaborated by considering the reaction mechanism. The reaction involved 4 steps. (Step 1): the heterolytic dissociation of molecular hydrogen on the metallic Pd surface followed by the hydrogen spillover over the support. (Step 2): adsorption of bicarbonate intermediate generated under mild basic conditions. (Step 3): nucleophilic reduction of bicarbonate to formate. (Step 4): desorption of formate product accompanied by water production, an initial active species [82]. Considering this mechanism, the

49

role of oxygen vacancies in the mobilization and stabilization of bicarbonate ions which act as intermediate, is prominent. The bicarbonate ions are mobilized and stabilized via oxygen vacancies, followed by their reduction with hydrogen, which is spilled over the support after dissociation at the Pd surface.

The effect of catalyst support on the hydrogenation and dehydrogenation activity was also investigated (**Table 3.1**). The results show that the $Pd1.5/ZrO_2$ performs poorly in hydrogenation and dehydrogenation. Compared to carbon support, the metal oxide support provides good electron mobility towards the metal with a narrow band gap due to oxygen vacancies. It might be due to the shallow specific surface area offering less dispersion. Another factor that might be decisive is the oxygen vacancy formation energies. Bridging oxygen vacancies provides anchoring sites to Pd with strong metal-support interaction to avoid agglomeration. The zirconia support has comparatively higher oxygen vacancy formation energies due to stable (sub)surface active oxygen, resulting in less (reverse)hydrogen spillover. Oxygen vacancies enable the (reverse) hydrogen transport and provide adsorption sites to reaction intermediates. The zirconia support seems to be stable compared to carbon support. However, ceria and titania are active supports in hydrogenation and dehydrogenation. Compared to zirconia and ceria, the titania provides (reverse) hydrogen transport at mild conditions as required in the bicarbonate-formate system. Due to oxygen vacancy formation at mild conditions, titania simultaneously provides vacancy and acid-base properties during reactions. In ceria, the surface oxygen is less active and mobile than titania in mild conditions; therefore, it may only involve acid-base properties during reactions. Ceria also suffers from dissolution issues and is very sensitive to reaction pH, leading to stability challenges [131].
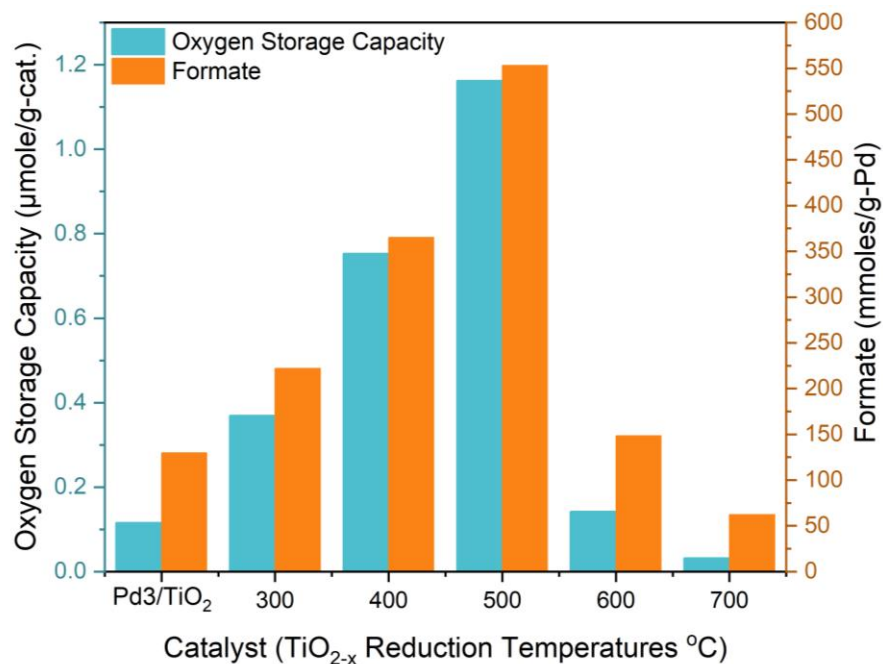
Figure 3.14. Relationship between the activity and the oxygen storage capacity of different catalysts.

Reaction Conditions (Hydrogenation): catalyst loading (100 mg), ammonium bicarbonate (1M, 20 mL), reaction time (10 mins), temperature (25 $^{\circ}$C), H_2 pressure (500 psi), stirring speed (350 rpm), and purging with pure N_2 (3 times).

Table 3.1. Effect of catalyst support on the (ammonium)bicarbonate-formate (de)hydrogenation activity.

Catalysts	Ammonium Formate Production (M/ g-Pd.h)	H_2 Production (L/g-Pd.h)
Pd1.5/ZrO$_2$	28	73
Pd2/CeO$_2$	240	154
Pd1.5/TiO$_{2-x}$ – 500 $^{\circ}$C	166	305

3.8. Hydrogenation – Dehydrogenation Reaction Kinetics

The best-performed catalyst, i.e., Pd3/TiO$_{2-x}$ – 500 ^{o}C, was selected for the detailed kinetic study for the (ammonium)bicarbonate – formate system. in case of hydrogenation, a wide range of ammonium bicarbonate concentrations and temperatures were selected. In case of dehydrogenation, time vs. temperature study has been carried out to investigate the kinetic parameters. The results are provided in (**Figure 3.17**). The results revealed that the first-order kinetics followed the reaction at all temperatures and then moved to the zero-order reaction when the solubility limits were reached in case of ammonium bicarbonate hydrogencation. The solubility of ammonium bicarbonate at room temperature is relatively low, and it decomposes into ammonia and carbon dioxide upon heating above 35 ^{o}C to increase the solubility [44]. Therefore, we investigated the hydrogenation kinetics below the decomposition temperature. From the results, the rate becomes constant at 10 ^{o}C after the 2M concentration of ammonium bicarbonate which is the solubility limit at this temperature. Higher than 2M concentration is a supersaturated solution. At supersaturation, ammonium bicarbonate concentration is constant at identical reaction conditions; the rate becomes constant, indicating the zero-order reaction (**Figure 3.15**). The reaction depends on the pH due to the equilibrium between the carbonate and bicarbonate ions. The hydrogenation of bicarbonate salts is easier compared to the carbonate ions as the rate-limiting step in the carbonate case is considered the protonation of carbonate ions. Carbonates have a lower tendency to exchange oxygen with water compared to bicarbonates [132]. Furthermore, at higher pH, the equilibrium shifts from bicarbonate to carbonate ions which restricts the high formate yield in the product [132]. From the results, introducing oxygen vacancies helps increase the number of active sites in terms of higher Pd dispersion, significantly reducing the reaction energy barrier. The dehydrogenation rate was found to be directly proportional to the reaction temperature (**Figure**

3.16). Another interesting observation is the reduction in the Pd3/TiO$_{2-x}$ – 500 °C reaction rates in both cases. The trade-off between the enthalpic and entropic effects could explain it. It is well admitted that the catalyst design is usually based on the enthalpic results, i.e., reduction in the energy barrier for a specific reaction, while completely ignoring the other side, i.e., entropic effects, mainly due to the confinement of metallic nanoparticles by the support [133]. In other words, introducing oxygen vacancies in reducible metal oxides results in the strong metal-support interaction (SMSI) phenomenon leading to confining of metal nanoparticles. It positively stabilizes the nanoparticles, reducing the possibility of agglomeration and increasing active sites due to higher dispersion. The drawback is that it reduces the free space around the nanoparticles to adsorb the intermediate species for a surface reaction. Such contribution may lead to a reduction in the reaction rates and activation energy simultaneously.
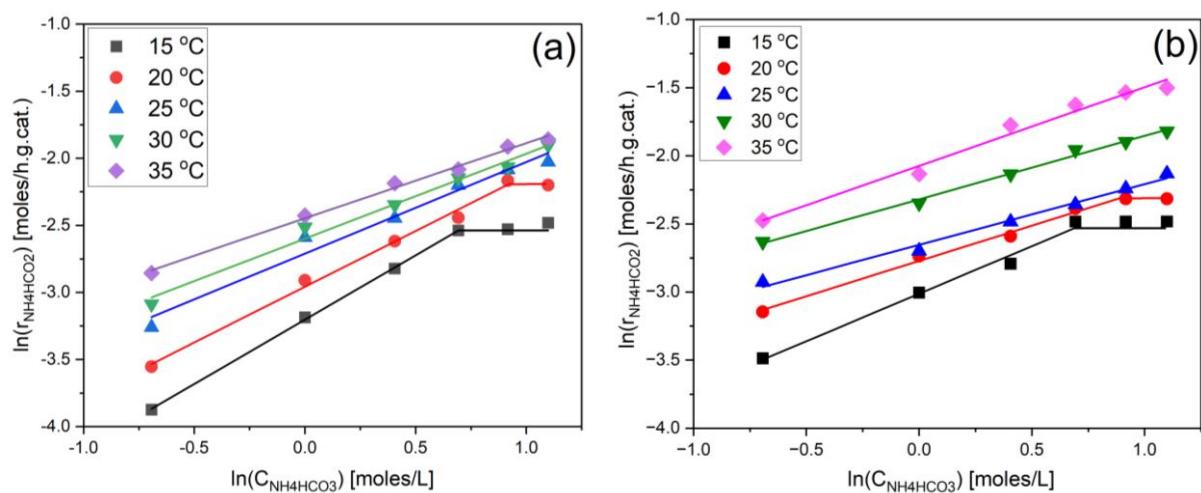
Figure 3.15. First order kinetics (concentration vs. rate) of ammonium bicarbonate hydrogenation over (a): Pd3/TiO$_{2-x}$ – 500 °C and (b): Pd3/TiO$_2$.
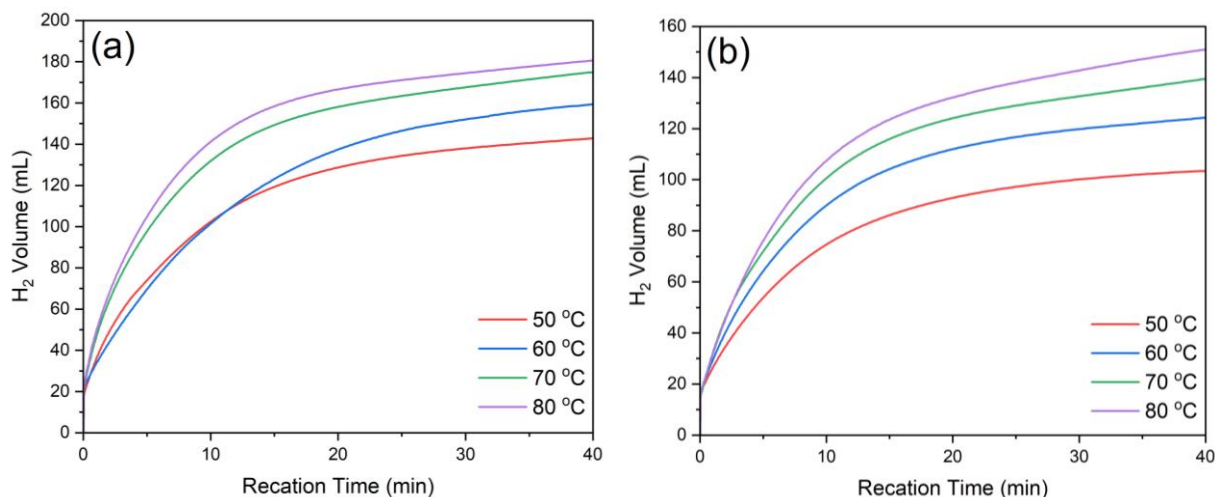
Figure 3.16. Ammonium formate dehydrogenation at different temperatures over (a): Pd3/TiO$_{2-x}$

– 500 ^{o}C and (b): Pd3/TiO$_2$.
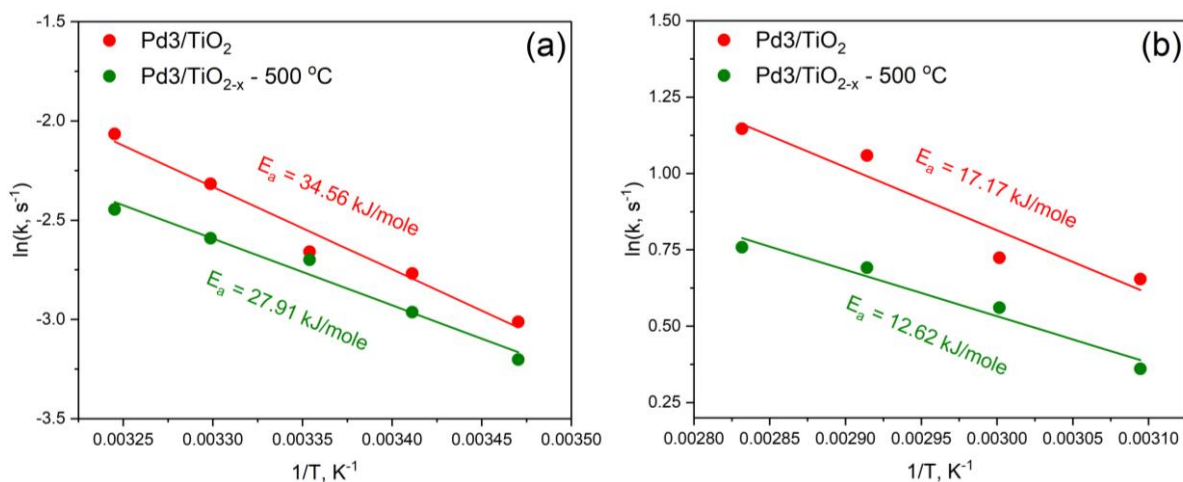
Figure 3.17. Kinetics of (ammonium)bicarbonate-formate system over the Pd3/TiO$_2$ and

Pd3/TiO$_{2-x}$ – 500 ^{o}C catalysts. (a): Hydrogenation and (b): Dehydrogenation.

Reaction Conditions: *Hydrogenation*: catalyst loading (50 mg), ammonium bicarbonate (1M, 20

mL), reaction time (10 mins), temperature (15 ^{o}C – 35 ^{o}C), H$_2$ pressure (500 psi), stirring speed

(350 rpm), and purging with pure N$_2$ (3 times). *Dehydrogenation*: catalyst loading (50 mg),

ammonium formate (1M, 20 mL), reaction time (40 mins), temperature ($50\ ^{o}C - 80\ ^{o}C$), stirring

speed (350 rpm), and purging with pure N_2 (3 times).

3.9. Hydrogenation – Dehydrogenation at Higher Concentrations

The selected catalyst was employed for hydrogenating ammonium bicarbonate at supersaturated conditions (**Table 3.2**). Due to the lower solubility of ammonium bicarbonate at room temperature and thermal instability at temperatures higher than $35\ ^{o}C$ in water, the solution became slurry when 5M and 7M solutions were prepared (**Figure 3.18**). The catalyst was active and stable and hydrogenated the slurry over a prolonged period without losing the active sites. Initially, the reaction rate was slow, probably due to the mass transfer resistances and higher pH. Still, formate was produced as the reaction proceeded forward, and bicarbonate dissolved, eliminating the mass transfer resistance; the reaction rate increased rapidly. After 30 hours, 65% conversion was achieved for 7M ammonium bicarbonate hydrogenation to ammonium formate. Similarly, the dehydrogenation of ammonium formate at higher concentration was carried out using the selected catalyst and 40% conversion was achieved in 1 hour without losing the hydrogen production rate (**Figure 3.19**).

Table 3.2. Summary of ammonium bicarbonate hydrogenation at supersaturated conditions.

Catalyst	Weight (mg)	H_2 (psi)	t (h)	T (^{o}C)	AB Conc. (M)	AF Conc. (M)
Pd3/TiO$_{2-x}$ – 500 ^{o}C	100	500	3	25	5	0.14
	300	500	3	25	5	0.38
	300	900	14	25	5	0.57

	300	900	24	25	5	0.81
	300	900	48	25	5	3.41
	300	900	72	25	5	3.84
	950	1000	30	35	7	4.70
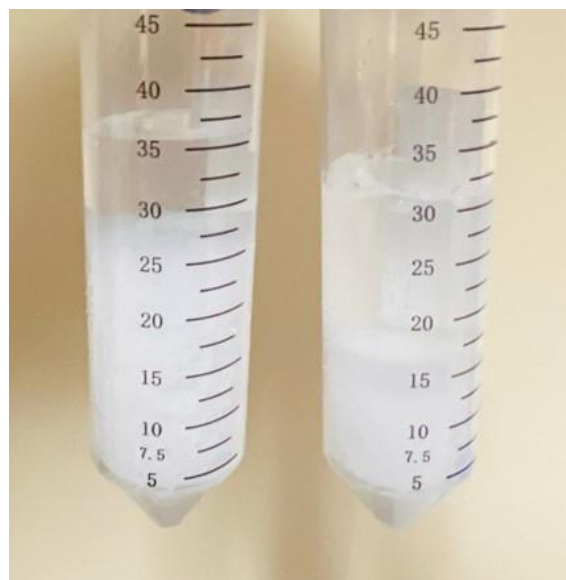
Figure 3.18. Slurry of ammonium bicarbonate for (left): 7M and (right): 5M solution in DI water.
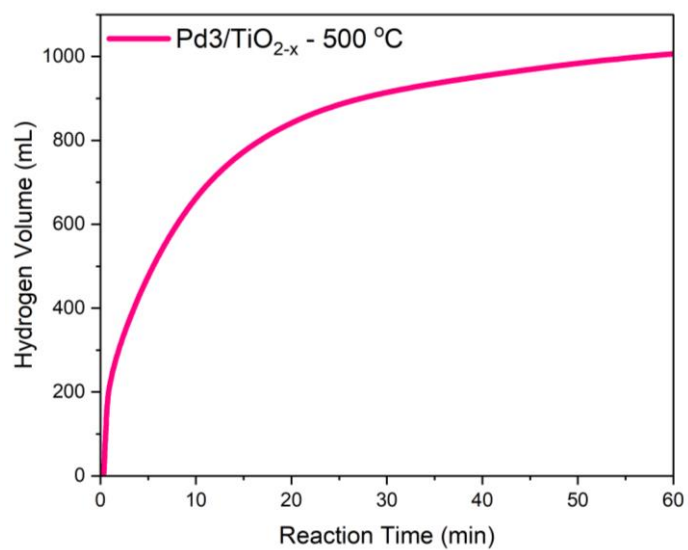
Figure 3.19. Ammonium formate dehydrogenation at higher concentrations of 5M.

: catalyst loading (300 mg), ammonium formate (5M, 20 mL), reaction time

(60 mins), temperature (80 ^oC), stirring speed (350 rpm), and purging with pure N_2 (3 times).

3.10. Mechanism of Hydrogenation – Dehydrogenation

To elucidate the possible mechanism of the (ammonium)bicarbonate-formate

(de)hydrogenation system, the in-situ ATR-FTIR analysis has been performed over the Pd3/TiO$_{2-}$

$_x$ – 500 ^oC, TiO$_{2-x}$ – 500 ^oC, and Pd nanoparticles. The aim was to probe the active sites of either

reaction on nanoparticles, support, and interface. In this regard, (**Figure 3.20**) showed the in-situ

ATR-FTIR for ammonium bicarbonate hydrogenation at ambient temperature and pressure

acquired over catalyst for 1 hour (10 minutes per spectra, excluding the baseline). Initially, we can

see the characteristic peaks of the ammonium bicarbonate located at 1303 and 1360 cm^{-1}.

Additionally, another region was observed within the range of 1450-1439 cm$^{-1,}$ which represented

the N-H vibrations and overlapped with ammonium formate, as ammonium is present in both

bicarbonate and formate. However, as the reaction proceeded in the forward directions, a peak

separation can be observed, and a new peak appeared from the N-H vibration indicating the

formation of ammonium formate due to ammonium bicarbonate hydrogenation. The intensity of

the peaks of ammonium bicarbonate decreased with time, indicating the consumption of reactants

and the formation of products. The bicarbonate peak around 1450 cm^{-1} showed a blue shift to 1439

cm$^{-1,}$ while the formate peak showed a red shift from 1450 cm^{-1} to 1496 cm^{-1}. It indicates that the

electrons are transferred from bicarbonate to formate. compared to Pd3/TiO$_{2-x}$ – 500 ^oC, no

ammonium formate peak was observed in TiO$_{2-x}$ – 500 ^oC (**Figure 3.21**) and Pd nanoparticles

(**Figure 3.22**). It indicates the lack of hydrogen activation in TiO$_{2-x}$ – 500 ^oC and intermediate

adsorption over Pd nanoparticles. The negative peaks in Pd nanoparticles indicate a decrease in

concentration at or near the surface and the –OH signals. In the case of ammonium formate

dehydrogenation, a similar trend was observed. In the case of Pd3/TiO$_{2-x}$ – 500 $^{\circ}$C (**Figure 3.23**), initially, a prominent peak of ammonium formate can be observed at 1690 cm^{-1}, which disappears over time as the reaction proceeded into the forward directions and the peak intensity of the bicarbonate region, mainly 1450 cm^{-1} get increased. Like hydrogenation, no product formation was observed on the TiO$_{2-x}$ – 500 $^{\circ}$C (**Figure 3.24**) and Pd nanoparticles (**Figure 3.25**).

Typically, in dehydrogenation, the lone pair of oxygen in the formate is supposed to be adsorbed on the oxygen-deficient site of the TiO$_{2-x}$, followed by the nucleophilic attack by the lone pair of water on the C atom to dissociate the C-H bond in formate and to form the bicarbonate. The hydrogen atom moved towards the Pd site with the reverse hydrogen spillover, where it combined with another hydrogen coming from ammonium ion to release the molecular hydrogen. During this process, the C-H bond dissociation is a rate-limiting step. The ammonia and CO$_2$ produced in this process are captured by the concentrated sodium hydroxide (NaOH) solution. In hydrogenation, the molecular hydrogen is supposed to dissociate heterolytically on the Pd site parallel with the adsorption of a lone pair of oxygen in the bicarbonate to the electron-deficient site of the TiO$_{2-x}$. The subsequent nucleophilic attack by the hydrogen at the C atom of the bicarbonate results in the -OH elimination with the formation and release of formate. Finally, water is produced and eliminated from the catalyst. The nucleophilic attack of the hydrogen on the carbonate's C atom is considered the rate-limit step (**Figure 3.26**).
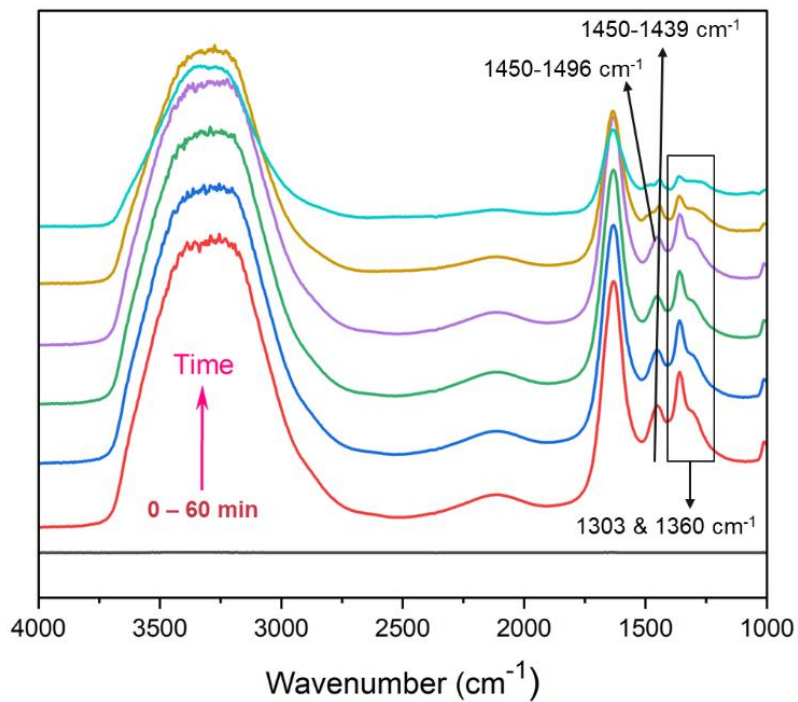
Figure 3.20. In-situ ATR – FTIR spectra of ammonium bicarbonate hydrogenation over Pd3/TiO$_{2-x}$ – 500 ^{o}C.
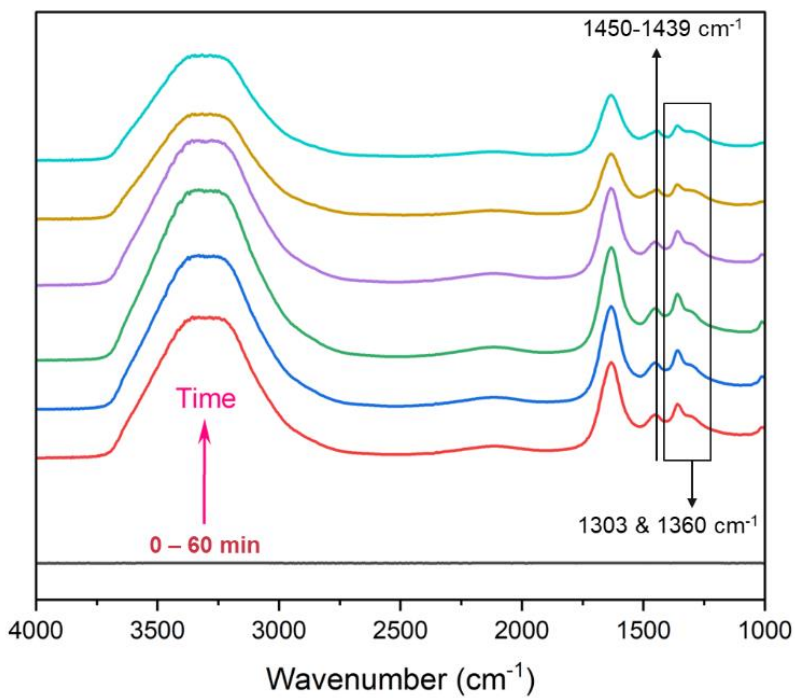
Figure 3.21. In-situ ATR – FTIR spectra of ammonium bicarbonate hydrogenation over TiO$_{2-x}$ – 500 ^{o}C.
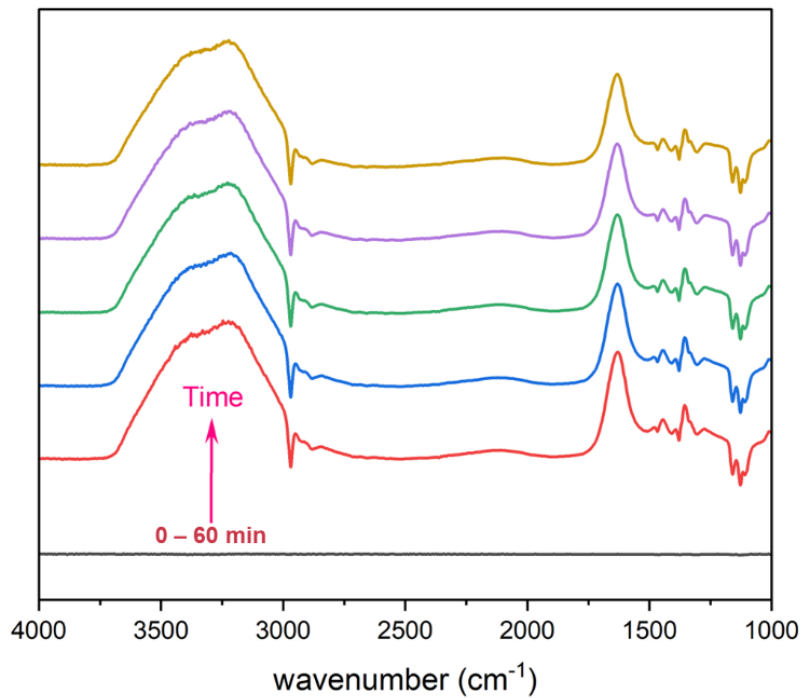
Figure 3.22. In-situ ATR – FTIR spectra of ammonium bicarbonate hydrogenation over Pd nanoparticles.
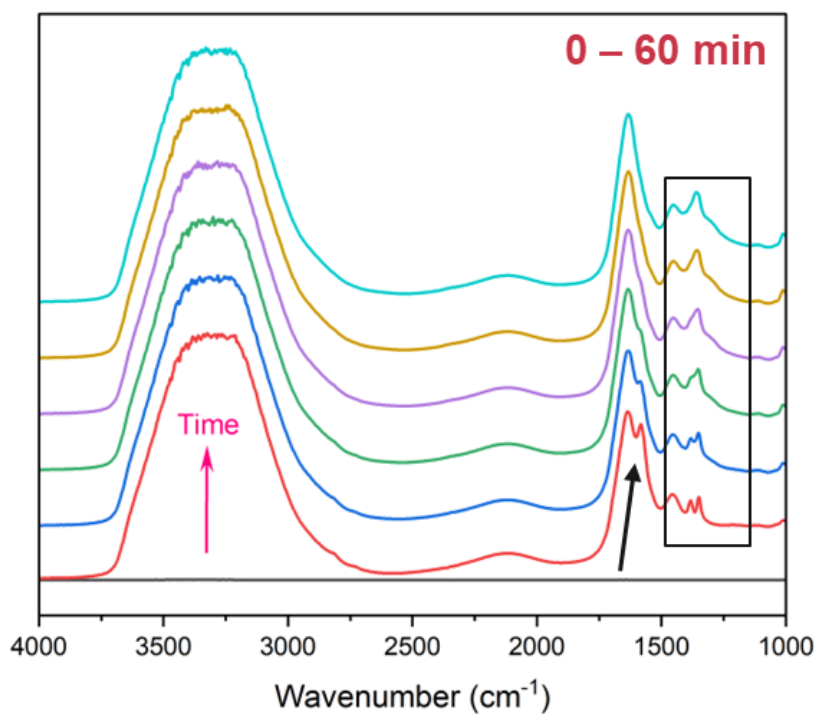
Figure 3.23. In-situ ATR – FTIR spectra of ammonium formate dehydrogenation over Pd3/TiO$_{2-x}$ − 500 $^{\circ}$C.
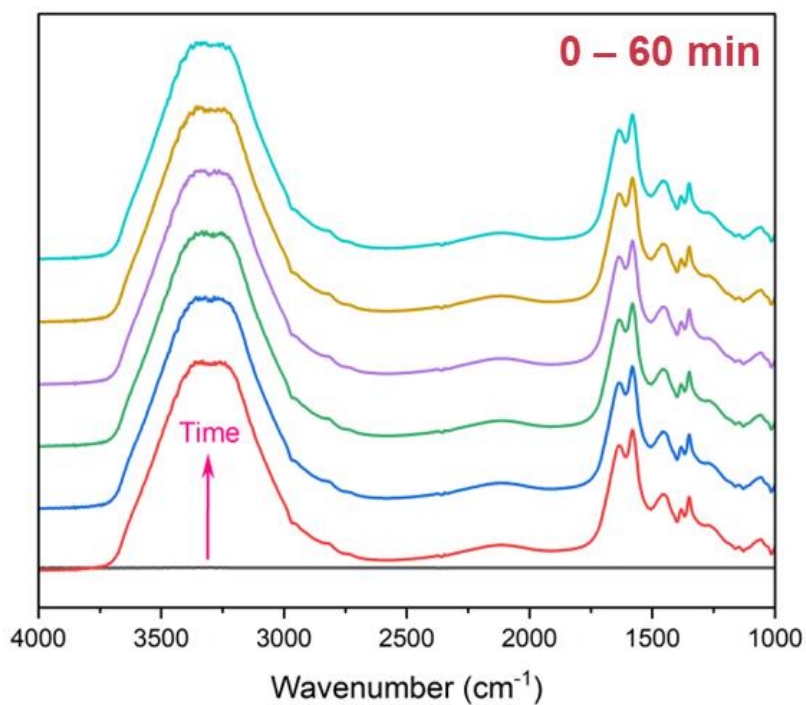
Figure 3.24. In-situ ATR – FTIR spectra of ammonium formate dehydrogenation over TiO_{2-x} – 500 °C.
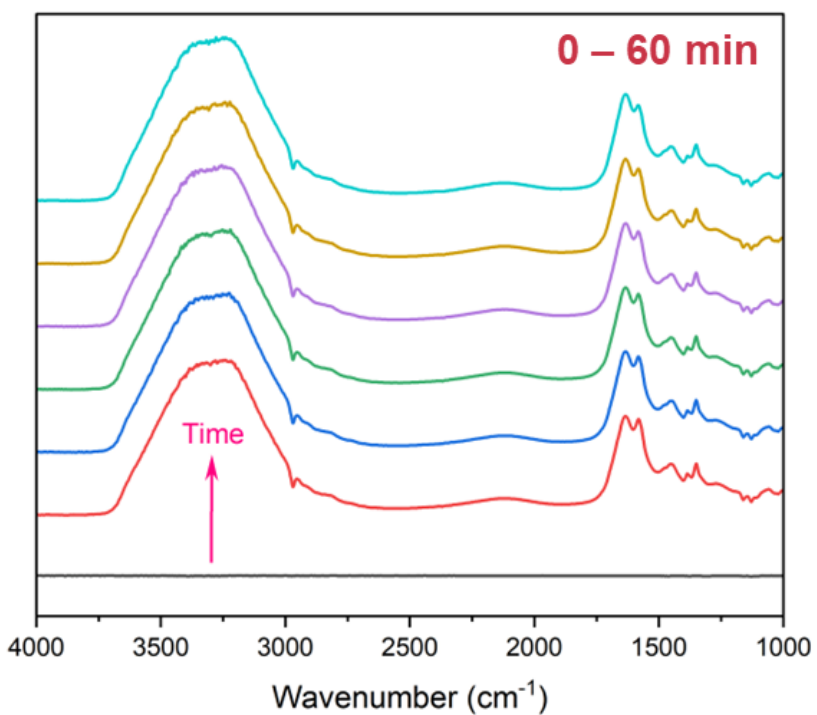
Figure 3.25. In-situ ATR – FTIR spectra of ammonium formate dehydrogenation over Pd nanoparticles.
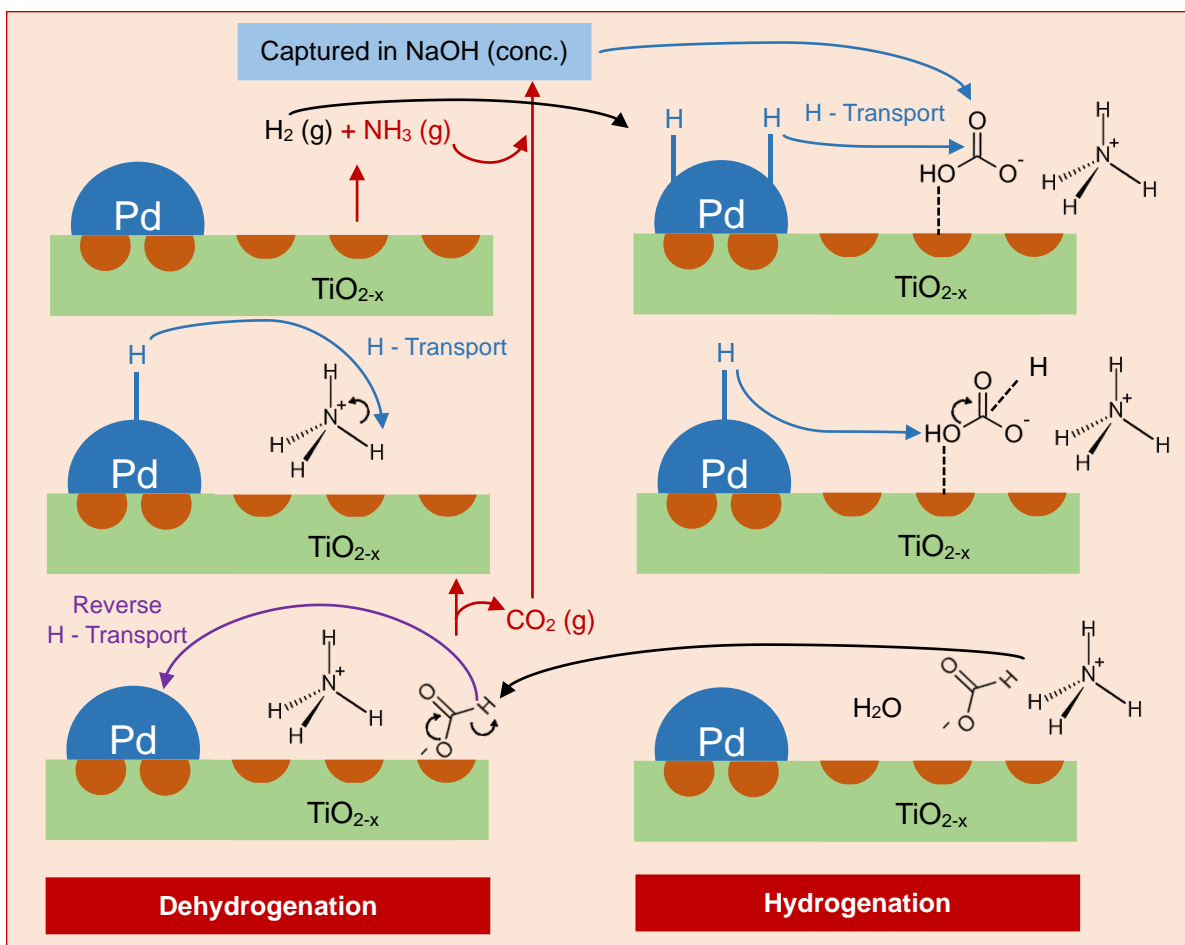
Figure 3.26. A schematic illustration of possible (ammonium)bicarbonate-formate (de)hydrogenation mechanism over Pd3/TiO$_{2-x}$ – 500 °C catalyst.

3.11.   Stability of Catalyst in Hydrogenation – Dehydrogenation

Followed by the detailed kinetic study, the best-performed catalyst, i.e., Pd3/TiO$_2$ – 500 °C, was subjected to long-term stability analysis in hydrogenation and dehydrogenation (**Figure 3.27**). In a typical run, a known amount of catalyst was loaded into the reactor with ammonium bicarbonate (1M, 30 mL). It was followed by purging with nitrogen (N$_2$) 3 times and H$_2$ charging at 500 psi for 10 minutes. In dehydrogenation, a known amount of catalyst was dispersed into 10 mL of DI water and charged into the reactor. The reactor was subjected to heating up to 80 °C after

purging it with nitrogen (N2) 3-times. Once the desired temperature was reached, 10 mL of ammonium formate (2M) was injected to make the overall concentration and volume into the reactor 1M and 20 mL, respectively.
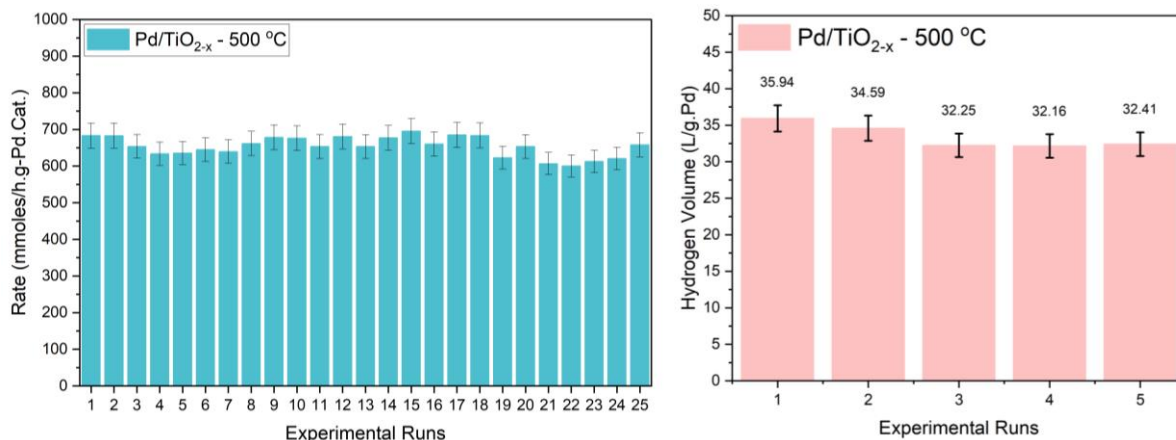
Figure 3.27. *(Left):* Long-term, i.e., 25 runs stability of the ammonium bicarbonate hydrogenation over Pd/TiO$_{2-x}$ – 500 $^{\circ}$C. *(Right):* Stability of Pd3/TiO$_{2-x}$ – 500 $^{\circ}$C for ammonium formate dehydrogenation.

<u>Reaction Conditions:</u> *(Hydrogenation)* ammonium bicarbonate (1M, 30 mL), hydrogen pressure (500 psi), temperature (25 $^{\circ}$C), reaction time (10 minutes), and stirring speed (350 rpm).

<u>Reaction Conditions:</u> *(Dehydrogenation)* ammonium formate (1M, 20 mL), temperature (80 $^{\circ}$C), reaction time (40 minutes per run), and stirring speed (350 rpm).

The generation of H$_2$ was monitored and recorded through a flowmeter for 40 minutes each run. After the reaction (hydrogenation), the liquid sample was filtered out for HPLC analysis, and the collected catalyst was subjected to the next run with identical conditions. It is well known that there is some catalyst loss in each run. After the 25th run, the spent catalyst was dried and weighed, and average weight loss was considered in each run to normalize the data. In such a case, the

catalyst demonstrated stability without adding fresh makeup catalyst to maintain the activity in hydrogenation and dehydrogenation. The results revealed that the catalyst loss activity but maintained based on the remaining catalyst over 25 runs in hydrogenation (with conversion about 2%, as the reaction is slow at initial stages, i.e., 10 minutes) and 5 runs in dehydrogenation (with conversion about 65%).

3.12. Summary of Hydrogenation – Dehydrogenation Catalysts

We synthesized a series of catalysts supported on carbon, metal-organic frameworks (MOFs), and metal oxide supports for efficient (de)hydrogenation of the (ammonium)bicarbonate-formate system. We found that the catalyst supported on carbon was highly active due to higher Pd dispersion and a high surface area of support. Unfortunately, it was not stable due to weaker metal-support interactions. Our previous work found that the Pd on carbon support is mobile and results in agglomeration, which could be a possible reason for the catalyst deactivation [134].
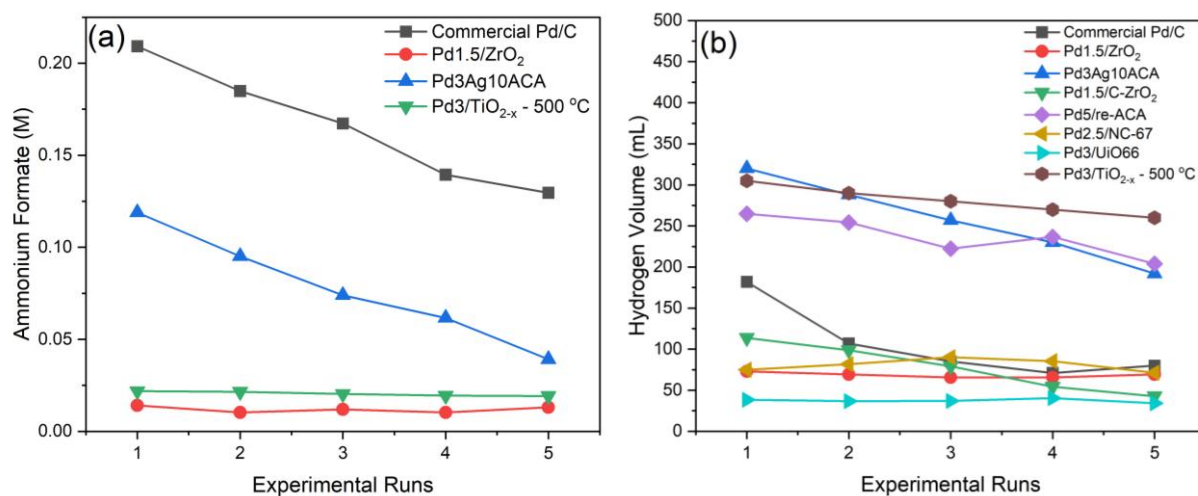
Figure 3.28. (Ammonium)bicarbonate-formate (de)hydrogenation over different catalysts. (a): Hydrogenation and (b): Dehydrogenation.

Reaction Conditions: *Hydrogenation:* Commercial Pd/C (5 wt.% Pd): Pd/C (50 mg), time (30 min), temperature (ambient temperature), H_2 Pressure (500 psi), and Mixing speed (400 rpm, approximately), *Pd1.5ZrO$_2$:* Pd1.5/ZrO$_2$ (200 mg), time (60 min), temperature (30 ^{o}C), H_2 Pressure (900 psi), and Mixing speed (400 rpm, approximately), Pd3Ag10ACA: Pd3Ag10ACA (50 mg), time (30 min), ambient temperature, H_2 Pressure (500 psi), and Mixing speed (400 rpm, approximately), and Pd3/TiO$_{2-x}$ – 500 ^{o}C: catalyst loading (50 mg), ammonium bicarbonate (1M, 20 mL), reaction time (10 mins), temperature (15 ^{o}C – 35 ^{o}C), H_2 pressure (500 psi), stirring speed (350 rpm), and purging with pure N_2 (3 times). *Dehydrogenation:* Commercial Pd/C (5 wt.% Pd): (50 mg), time (20 min), temperature (50 ^{o}C), and Mixing speed (400 rpm, approximately), *Pd1.5ZrO$_2$:* Pd1.5/ZrO$_2$ (200 mg), time (20 min), temperature (50 ^{o}C), and Mixing speed (400 rpm, approximately), Pd3Ag10ACA, Pd5/re-ACA, and Pd1.5/C-ZrO$_2$, Pd2.5/NC-67: Pd3Ag10ACA (50 mg), ammonium formate (1M, 20 mL), temperature (80 ^{o}C), time (20 min), and N_2 purging, Pd3/UiO66 and Pd3/TiO$_{2-x}$ – 500 ^{o}C: catalyst loading (50 mg), ammonium formate (1M, 20 mL), reaction time (40 mins), temperature (80 ^{o}C), stirring speed (350 rpm), and purging with pure N_2 (3 times).

Therefore, we considered the metal oxide support, which initially has lower activity due to less specific surface area and less Pd dispersion but is stable due to good electron mobility from support to metal and provides strong metal-support interactions. A summary of developed catalysts for (de)hydrogenation of the (ammonium)bicarbonate-formate system is provided in (**Figure 3.28**).

3.13. Density Functional Theory (DFT) Calculations

Metal support interaction is evident from the Bader charge calculations across the Pd3/TiO$_2$ catalyst (**Figure 3.29**) and the Pd3/TiO$_{2-x}$ – 500 °C surfaces (**Figure 3.31**). The interface with oxygen vacancies on TiO$_2$ shows a negative charge on Pd of magnitude |1.6 e$^-$|, suggesting the Pd nanoparticles receive extra electrons (**Figure 3.32**). While the pristine TiO$_2$ surface without O vacancies shows the reverse phenomena where the charge is transferred away from the Pd clusters as the Pd acquires a positive charge of |0.7 e$^-$| (**Figure 3.30**). Consequently, the adsorption energies of the catalytic reactants are severely affected. For example, the dissociative H$_2$ adsorption over the interface weakens by approximately 0.74 eV due to extra charge accumulation on Pd (for the Pd3/TiO$_{2-x}$ – 500 °C). The adsorption energies of the formate and the bicarbonate species also weaken by approximately 0.85 eV. The decreased adsorption energies can explain the compromised pre-exponential factor over the Pd3/TiO$_{2-x}$ – 500 °C compared to the base catalyst Pd3/TiO$_2$. As for the lowered hydrogenation activation barriers in the presence of vacancies, that can be explained by the lowering of H$_2$ spillover energetics from Pd to O atoms of TiO$_2$ at the interface. The energetics lower by approximately 0.17 eV over the Pd3/TiO$_{2-x}$ – 500 °C surface relative to the Pd3/TiO$_2$.

Moreover, the interface makes the dissociative H$_2$ adsorption easier by 0.12 eV (-0.74 eV vs. -0.6 eV on a clean Pd(111) surface). It makes the interface (with vacancies) readily active, supplying adsorbed H* for hydrogenation and dehydrogenation (recombining to form H$_2$). A more comprehensive effect of these interfacial behaviors of the reactants can only be simulated via thorough microkinetic modeling. Nevertheless, the DFT results qualitatively align with the experimental implications of the metal support interaction via the presence of oxygen vacancies (**Table 3.3**).
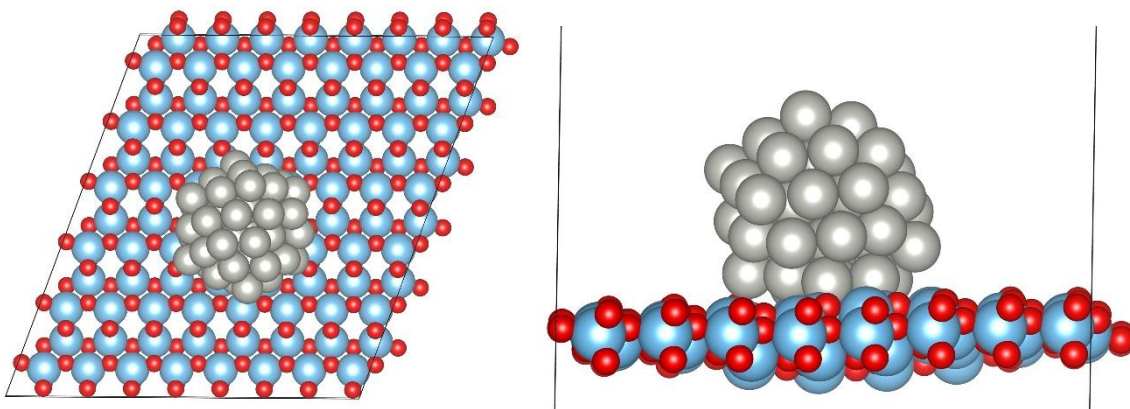
Figure 3.29. Pd deposited over the pristine TiO_2, i.e., Pd_{55}/TiO_2. *(Left):* Top view and *(Right):* Side view.
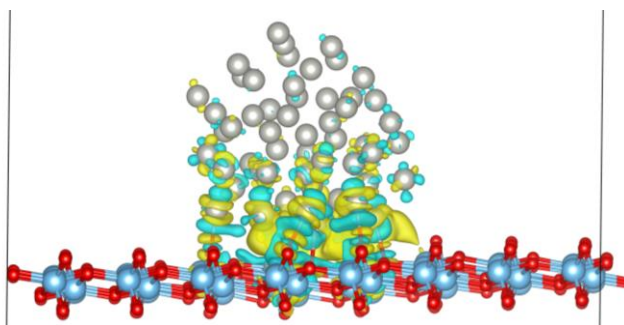
Figure 3.30. Charge transfer from Pd to pristine TiO_2. Yellow indicates regions of electron depletion, and cyan indicates regions of electron accumulation.
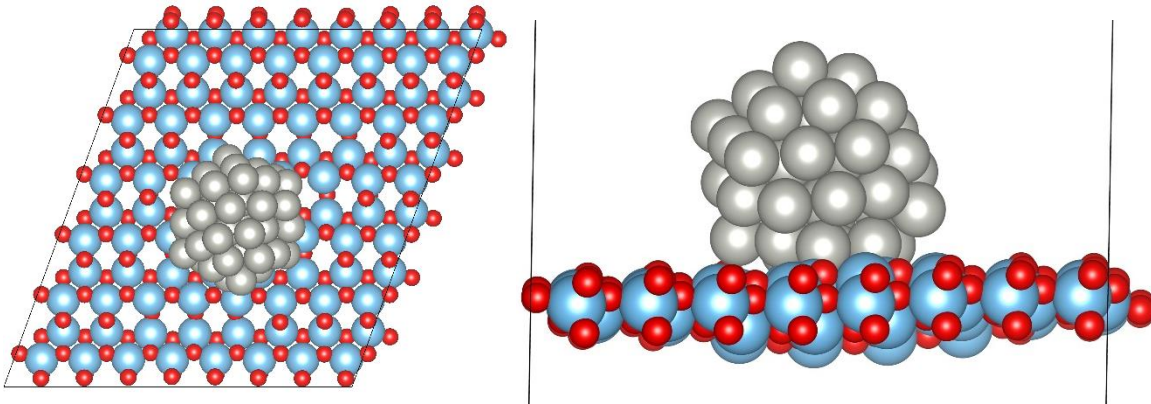
Figure 3.31. Pd deposited over the reduced TiO_{2-x} (12 O_v, 4×4 around Pd nanoparticles), i.e.,

Pd_{55}/TiO_2. *(Left):* Top view and *(Right):* Side view.
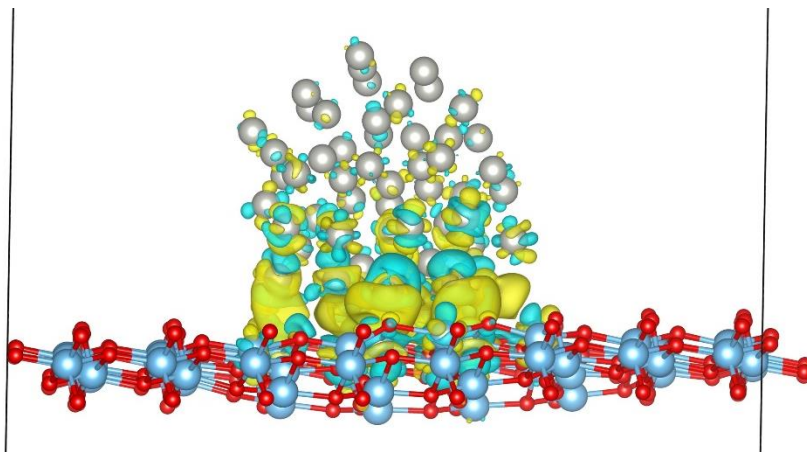
Figure 3.32. Charge transfer from reduced TiO_{2-x} to Pd nanoparticles. Yellow indicates regions

of electron depletion, and cyan indicates regions of electron accumulation.

Table 3.3. Summary of DFT calculations for the adsorption energies of different species over pristine and oxygen vacancy defected TiO$_2$ supported Pd nanoparticles.

Adsorption (eV)	Pd clean	Pd55/TiO$_2$	Pd55/TiO$_{2-x}$	Discussions
H on Pd	-0.62	-0.74	-0.01	Higher electron density at Pd from support in vacancies results in strong metal support interaction, weakening the binding energies of H$_2$ on Pd.
H on Ti		-0.02	0.55	Higher electron density at Ti due to vacancies results in strong metal support interaction, which weakens the binding energies of H$_2$ on Ti.
Formate	-0.13	-0.48	0.46	Formate and bicarbonate (de)hydrogenation are more favorable on Pd55/TiO$_{2-x}$ as it has weaker binding energy and is easy to release product after reaction. In addition, the higher bicarbonate over Pd indicates that the support is the favorable adsorption site.
Bicarbonate	-2.34	-2.79	-1.94	
Charge on Pd (e$^-$)	0	-0.7	1.6	The positive value indicates that the charge is accumulating on Pd.

H₂ Transport Energy (Pd to Ti)		0.72	0.55	It indicates that the H_2 spillover is more favorable in vacancies as it has a lower energy of 0.55 eV than the pristine surface (0.72 eV).

CHAPTER 4: CONCLUSION AND FUTURE WORK

In this work, we synthesized the defective titania, i.e., oxygen vacancy-supported Pd catalysts, for efficient (de)hydrogenation of the (ammonium)bicarbonate-formate system. According to our knowledge, the first time, we optimized the activity of the catalyst by tuning the concentration of the oxygen vacancies by varying the reduction temperatures. The selected catalyst was active and stable in (de)hydrogenation of the (ammonium)bicarbonate-formate system. Compared to the reported literature, the catalyst developed in this work was more active with long-term stability. For the system investigated in this work, we proposed a method to identify the hydrogen spillover in liquid-phase reactions, which is mainly reported for gas-phase reactions in the literature. A detailed in-situ ATR study revealed that the catalyst interface is the active site for the (de)hydrogenation reactions. No signal was found for the Pd nanoparticles and support separately when investigated for (de)hydrogenation reactions. In the literature, there is conflict, and different research proposed different active sites, i.e., nanoparticle, support, or interface. Based on DFT calculations, a charge transfer from support to metal was observed due to the higher electron density over the support because of oxygen removal.

In terms of future work, based on our preliminary results, a bimetallic catalyst could be developed to investigate the simultaneous ligand effect, i.e., electron transfer effect and strain effect. More detailed and in-depth studies can be carried out on the role of water as a solvent and how it affects the surface properties of the catalyst and promotes the H_2 spillover. The mechanism of H_2 spillover in liquid phase reaction must be investigated in more detail.

REFERENCES

[1] Q. Lai *et al.*, "How to design hydrogen storage materials? Fundamentals, synthesis, and storage tanks," *Advanced Sustainable Systems,* vol. 3, no. 9, p. 1900043, 2019.

[2] S. Brenner, "The impact of society on science," *Science,* vol. 282, no. 5393, pp. 1411-1412, 1998.

[3] S. Şener and E. Sarıdoğan, "The effects of science-technology-innovation on competitiveness and economic growth," *Procedia-Social and Behavioral Sciences,* vol. 24, pp. 815-828, 2011.

[4] J. Smyth, "Science and technology education and future human needs," *Environmentalist,* vol. 6, no. 2, pp. 145-151, 1986.

[5] G. Kallis, C. Kerschner, and J. Martinez-Alier, "The economics of degrowth," vol. 84, ed: Elsevier, 2012, pp. 172-180.

[6] Ö. Esen and M. Bayrak, "Does more energy consumption support economic growth in net energy-importing countries?," *Journal of Economics, Finance and Administrative Science,* vol. 22, no. 42, pp. 75-98, 2017.

[7] A. Züttel, A. Remhof, A. Borgschulte, and O. Friedrichs, "Hydrogen: the future energy carrier," *Philosophical Transactions of the Royal Society A: Mathematical, Physical and Engineering Sciences,* vol. 368, no. 1923, pp. 3329-3342, 2010.

[8] I. Ridjan, B. V. Mathiesen, D. Connolly, and N. Duić, "The feasibility of synthetic fuels in renewable energy systems," *Energy,* vol. 57, pp. 76-84, 2013.

[9] S. H. Jensen, P. H. Larsen, and M. Mogensen, "Hydrogen and synthetic fuel production from renewable energy sources," *International Journal of Hydrogen Energy,* vol. 32, no. 15, pp. 3253-3257, 2007.

[10]   J. B. S. Haldane, *Daedalus or Science and the Future*. EP Dutton New York, 1924.

[11]   O. Cf, "Transforming our world: the 2030 Agenda for Sustainable Development," *United Nations: New York, NY, USA,* 2015.

[12]   J. B. Zimmerman, P. T. Anastas, H. C. Erythropel, and W. Leitner, "Designing for a green chemistry future," *Science,* vol. 367, no. 6476, pp. 397-400, 2020.

[13]   S. Kovalyshyn, O. Kaygusuz, and M. Guney, "Global energy demand and woody biomass," *Journal of Engineering Research and Applied Science,* vol. 8, no. 1, pp. 1119-1126, 2019.

[14]   D. Xu, G. Lin, S. Guo, S. Wang, Y. Guo, and Z. Jing, "Catalytic hydrothermal liquefaction of algae and upgrading of biocrude: A critical review," *Renewable and Sustainable Energy Reviews,* vol. 97, pp. 103-118, 2018.

[15]   V. Trombettoni, F. Campana, A. Marrocchi, and L. Vaccaro, "Sustainable Batch or Continuous-flow Preparation of Biomass-derived Fuels Using Sulfonated Organic Polymers," 2019.

[16]   W. Fang and A. Riisager, "Recent advances in heterogeneous catalytic transfer hydrogenation/hydrogenolysis for valorization of biomass-derived furanic compounds," *Green Chemistry,* vol. 23, no. 2, pp. 670-688, 2021.

[17]   Y. Li, W. Liu, Z. Zhang, X. Du, L. Yu, and Y. Deng, "A self-powered electrolytic process for glucose to hydrogen conversion," *Communications Chemistry,* vol. 2, no. 1, p. 67, 2019.

[18]   Y. Jing, Y. Guo, Q. Xia, X. Liu, and Y. Wang, "Catalytic production of value-added chemicals and liquid fuels from lignocellulosic biomass," *Chem,* vol. 5, no. 10, pp. 2520-2546, 2019.

[19]   L. Shuai and J. Luterbacher, "Organic solvent effects in biomass conversion reactions," *ChemSusChem,* vol. 9, no. 2, pp. 133-155, 2016.

[20]   H. Li *et al.*, "Carbon-increasing catalytic strategies for upgrading biomass into energy-intensive fuels and chemicals," *Acs Catalysis,* vol. 8, no. 1, pp. 148-187, 2018.

[21]   A. Corma, S. Iborra, and A. Velty, "Chemical routes for the transformation of biomass into chemicals," *Chemical reviews,* vol. 107, no. 6, pp. 2411-2502, 2007.

[22]   Z. Sun *et al.*, "Complete lignocellulose conversion with integrated catalyst recycling yielding valuable aromatics and fuels," *Nature catalysis,* vol. 1, no. 1, pp. 82-92, 2018.

[23]   H. Wang, Y. Yang, and L. Guo, "Renewable-biomolecule-based electrochemical energy-storage materials," *Advanced Energy Materials,* vol. 7, no. 23, p. 1700663, 2017.

[24]   H. Wang, S. Zhang, X. Bi, and R. Clift, "Greenhouse gas emission reduction potential and cost of bioenergy in British Columbia, Canada," *Energy Policy,* vol. 138, p. 111285, 2020.

[25]   F. Valentini, A. Marrocchi, and L. Vaccaro, "Liquid Organic Hydrogen Carriers (LOHCs) as H-Source for Bio-Derived Fuels and Additives Production," *Advanced Energy Materials,* vol. 12, no. 13, p. 2103362, 2022.

[26]   G. P. Peters, G. Marland, C. Le Quéré, T. Boden, J. G. Canadell, and M. R. Raupach, "Rapid growth in CO2 emissions after the 2008–2009 global financial crisis," *Nature climate change,* vol. 2, no. 1, pp. 2-4, 2012.

[27]   R. Aslam, K. Müller, M. Müller, M. Koch, P. Wasserscheid, and W. Arlt, "Measurement of hydrogen solubility in potential liquid organic hydrogen carriers," *Journal of chemical & engineering data,* vol. 61, no. 1, pp. 643-649, 2016.

[28]   K. Mazloomi and C. Gomes, "Hydrogen as an energy carrier: Prospects and challenges," *Renewable and Sustainable Energy Reviews,* vol. 16, no. 5, pp. 3024-3033, 2012.

[29]   R. B. Gupta, *Hydrogen fuel: production, transport, and storage*. CRC press, 2008.

[30]   A. Züttel, "Materials for hydrogen storage," *Materials today,* vol. 6, no. 9, pp. 24-33, 2003.

[31]   K. Müller and W. Arlt, "Status and development in hydrogen transport and storage for energy applications," *Energy technology,* vol. 1, no. 9, pp. 501-511, 2013.

[32]   A. Iulianelli and A. Basile, *Advances in hydrogen production, storage and distribution.* Elsevier, 2014.

[33]   https://www.hydrogen.energy.gov/pdfs/review20/st204_autrey_2020_o.pdf.

[34]   M. Markiewicz *et al.*, "Environmental and health impact assessment of Liquid Organic Hydrogen Carrier (LOHC) systems–challenges and preliminary results," *Energy & Environmental Science,* vol. 8, no. 3, pp. 1035-1045, 2015.

[35]   N. Brückner *et al.*, "Evaluation of Industrially applied heat-transfer fluids as liquid organic hydrogen carrier systems," *ChemSusChem,* vol. 7, no. 1, pp. 229-235, 2014.

[36]   D. Teichmann, K. Stark, K. Müller, G. Zöttl, P. Wasserscheid, and W. Arlt, "Energy storage in residential and commercial buildings via Liquid Organic Hydrogen Carriers (LOHC)," *Energy & Environmental Science,* vol. 5, no. 10, pp. 9044-9054, 2012.

[37]   D. Teichmann, W. Arlt, and P. Wasserscheid, "Liquid Organic Hydrogen Carriers as an efficient vector for the transport and storage of renewable energy," *International journal of hydrogen energy,* vol. 37, no. 23, pp. 18118-18132, 2012.

[38]   F. Sotoodeh and K. J. Smith, "An overview of the kinetics and catalysis of hydrogen storage on organic liquids," *The Canadian Journal of Chemical Engineering,* vol. 91, no. 9, pp. 1477-1490, 2013.

[39]   S. Kar, A. Goeppert, and G. S. Prakash, "Integrated CO_2 capture and conversion to formate and methanol: connecting two threads," *Accounts of chemical research,* vol. 52, no. 10, pp. 2892-2903, 2019.

[40] Z.-Z. Yang, L.-N. He, Y.-N. Zhao, B. Li, and B. Yu, "CO_2 capture and activation by superbase/polyethylene glycol and its subsequent conversion," *Energy & Environmental Science,* vol. 4, no. 10, pp. 3971-3975, 2011.

[41] Z.-Z. Yang, Y.-N. Zhao, and L.-N. He, "CO_2 chemistry: task-specific ionic liquids for CO2 capture/activation and subsequent conversion," *Rsc Advances,* vol. 1, no. 4, pp. 545-567, 2011.

[42] A. H. Liu *et al.*, "Equimolar CO_2 capture by N-substituted amino acid salts and subsequent conversion," *Angewandte Chemie International Edition,* vol. 51, no. 45, pp. 11306-11310, 2012.

[43] K. Grubel, H. Jeong, C. W. Yoon, and T. Autrey, "Challenges and opportunities for using formate to store, transport, and use hydrogen," *Journal of Energy Chemistry,* vol. 41, pp. 216-224, 2020.

[44] J. Su, L. Yang, M. Lu, and H. Lin, "Highly efficient hydrogen storage system based on ammonium bicarbonate/formate redox equilibrium over palladium nanocatalysts," *ChemSusChem,* vol. 8, no. 5, pp. 813-816, 2015.

[45] X. Chen, Y. Liu, and J. Wu, "Sustainable production of formic acid from biomass and carbon dioxide," *Molecular Catalysis,* vol. 483, p. 110716, 2020.

[46] V. F. Valdés-López, T. Mason, P. R. Shearing, and D. J. Brett, "Carbon monoxide poisoning and mitigation strategies for polymer electrolyte membrane fuel cells–A review," *Progress in Energy and Combustion Science,* vol. 79, p. 100842, 2020.

[47] D. Mellmann, P. Sponholz, H. Junge, and M. Beller, "Formic acid as a hydrogen storage material–development of homogeneous catalysts for selective hydrogen release," *Chemical Society Reviews,* vol. 45, no. 14, pp. 3954-3988, 2016.

[48]   J. H. Lee *et al.*, "Carbon dioxide mediated, reversible chemical hydrogen storage using a Pd nanocatalyst supported on mesoporous graphitic carbon nitride," *Journal of Materials Chemistry A,* vol. 2, no. 25, pp. 9490-9495, 2014.

[49]   Q. Y. Bi, J. D. Lin, Y. M. Liu, H. Y. He, F. Q. Huang, and Y. Cao, "Dehydrogenation of formic acid at room temperature: boosting palladium nanoparticle efficiency by coupling with pyridinic-nitrogen-doped carbon," *Angewandte Chemie International Edition,* vol. 55, no. 39, pp. 11849-11853, 2016.

[50]   K. Mori, S. Masuda, H. Tanaka, K. Yoshizawa, M. Che, and H. Yamashita, "Phenylamine-functionalized mesoporous silica supported PdAg nanoparticles: a dual heterogeneous catalyst for formic acid/CO_2-mediated chemical hydrogen delivery/storage," *Chemical Communications,* vol. 53, no. 34, pp. 4677-4680, 2017.

[51]   S. Masuda, K. Mori, Y. Futamura, and H. Yamashita, "PdAg nanoparticles supported on functionalized mesoporous carbon: promotional effect of surface amine groups in reversible hydrogen delivery/storage mediated by formic acid/CO_2," *ACS Catalysis,* vol. 8, no. 3, pp. 2277-2285, 2018.

[52]   M. Lu, J. Zhang, Y. Yao, J. Sun, Y. Wang, and H. Lin, "Renewable energy storage via efficient reversible hydrogenation of piperidine captured CO_2," *Green Chemistry,* vol. 20, no. 18, pp. 4292-4298, 2018.

[53]   Q. Sun *et al.*, "Zeolite-encaged Pd–Mn nanocatalysts for CO_2 hydrogenation and formic acid dehydrogenation," *Angewandte Chemie International Edition,* vol. 59, no. 45, pp. 20183-20191, 2020.

[54]   Q. Y. Bi *et al.*, "An aqueous rechargeable formate-based hydrogen battery driven by heterogeneous Pd catalysis," *Angewandte Chemie International Edition,* vol. 53, no. 49, pp. 13583-13587, 2014.

[55]   X. Shao *et al.*, "Pd@C_3N_4 nanocatalyst for highly efficient hydrogen storage system based on potassium bicarbonate/formate," *AIChE Journal,* vol. 62, no. 7, pp. 2410-2418, 2016.

[56]   F. Wang, J. Xu, X. Shao, X. Su, Y. Huang, and T. Zhang, "Palladium on nitrogen-doped mesoporous carbon: a bifunctional catalyst for formate-based, carbon-neutral hydrogen storage," *ChemSusChem,* vol. 9, no. 3, pp. 246-251, 2016.

[57]   K. Koh, M. Jeon, D. M. Chevrier, P. Zhang, C. W. Yoon, and T. Asefa, "Novel nanoporous N-doped carbon-supported ultrasmall Pd nanoparticles: Efficient catalysts for hydrogen storage and release," *Applied Catalysis B: Environmental,* vol. 203, pp. 820-828, 2017.

[58]   H. Zhong *et al.*, "Interconversion between CO_2 and HCOOH under basic conditions catalyzed by PdAu nanoparticles supported by amine-functionalized reduced graphene oxide as a dual catalyst," *ACS Catalysis,* vol. 8, no. 6, pp. 5355-5362, 2018.

[59]   K. Nakajima, M. Tominaga, M. Waseda, H. Miura, and T. Shishido, "Highly efficient supported palladium–gold alloy catalysts for hydrogen storage based on ammonium bicarbonate/formate redox cycle," *ACS Sustainable Chemistry & Engineering,* vol. 7, no. 7, pp. 6522-6530, 2019.

[60]   S. Masuda, Y. Shimoji, K. Mori, Y. Kuwahara, and H. Yamashita, "Interconversion of Formate/Bicarbonate for Hydrogen Storage/Release: Improved Activity Following Sacrificial Surface Modification of a Ag@ Pd/TiO_2 Catalyst with a TiO_x Shell," *ACS Applied Energy Materials,* vol. 3, no. 6, pp. 5819-5829, 2020.

[61]   Y. Chang, Y. Cheng, Y. Feng, K. Li, H. Jian, and H. Zhang, "Upshift of the d band center toward the Fermi level for promoting silver ion release, bacteria inactivation, and wound healing of alloy silver nanoparticles," *ACS applied materials & interfaces,* vol. 11, no. 13, pp. 12224-12231, 2019.

[62]   F. Gao and D. W. Goodman, "Pd–Au bimetallic catalysts: understanding alloy effects from planar models and (supported) nanoparticles," *Chemical Society Reviews,* vol. 41, no. 24, pp. 8009-8020, 2012.

[63]   X. Shao, X. Miao, T. Zhang, W. Wang, J. Wang, and X. Ji, "Pd nanoparticles supported on N-and P-Co-doped carbon as catalysts for reversible formate-based chemical hydrogen storage," *ACS Applied Nano Materials,* vol. 3, no. 9, pp. 9209-9217, 2020.

[64]   J. Zhang *et al.*, "Morphology-engineered highly active and stable Pd/TiO2 catalysts for CO2 hydrogenation into formate," *Journal of Catalysis,* vol. 405, pp. 152-163, 2022.

[65]   S. Matsuda and A. Kato, "Titanium oxide based catalysts-a review," *Applied Catalysis,* vol. 8, no. 2, pp. 149-165, 1983.

[66]   W. Chen, Q. Kuang, Q. Wang, and Z. Xie, "Engineering a high energy surface of anatase TiO_2 crystals towards enhanced performance for energy conversion and environmental applications," 2015.

[67]   T. L. Thompson and J. T. Yates, "Surface science studies of the photoactivation of TiO_2 new photochemical processes," *Chemical reviews,* vol. 106, no. 10, pp. 4428-4453, 2006.

[68]   M. Grätzel, "Photoelectrochemical cells," *nature,* vol. 414, no. 6861, pp. 338-344, 2001.

[69]   A. Dahal *et al.*, "Adsorption and reaction of methanol on anatase TiO2 (101) single crystals and faceted nanoparticles," *The Journal of Physical Chemistry C,* vol. 123, no. 39, pp. 24133-24145, 2019.

[70]   D. W. Goodman, "Correlations between surface science models and "real-world" catalysts," *The Journal of Physical Chemistry,* vol. 100, no. 31, pp. 13090-13102, 1996.

[71]   F. Gao and D. W. Goodman, "Model catalysts: simulating the complexities of heterogeneous catalysts," *Annual review of physical chemistry,* vol. 63, pp. 265-286, 2012.

[72]   C. T. Campbell, "Studies of model catalysts with well-defined surfaces combining ultrahigh vacuum surface characterization with medium-and high-pressure kinetics," *Advances in Catalysis,* vol. 36, pp. 1-54, 1989.

[73]   H.-J. Freund, H. Kuhlenbeck, J. Libuda, G. Rupprechter, M. Bäumer, and H. Hamann, "Bridging the pressure and materials gaps between catalysis and surface science: clean and modified oxide surfaces," *Topics in Catalysis,* vol. 15, pp. 201-209, 2001.

[74]   J. Fan *et al.*, "Recent progress on rational design of bimetallic Pd based catalysts and their advanced catalysis," *ACS Catalysis,* vol. 10, no. 22, pp. 13560-13583, 2020.

[75]   M. Valenti *et al.*, "Suppressing H_2 evolution and promoting selective CO_2 electroreduction to CO at low overpotentials by alloying Au with Pd," *ACS Catalysis,* vol. 9, no. 4, pp. 3527-3536, 2019.

[76]   N. Schweitzer, H. Xin, E. Nikolla, J. T. Miller, and S. Linic, "Establishing relationships between the geometric structure and chemical reactivity of alloy catalysts based on their measured electronic structure," *Topics in Catalysis,* vol. 53, pp. 348-356, 2010.

[77]   J. K. Nørskov, T. Bligaard, J. Rossmeisl, and C. H. Christensen, "Towards the computational design of solid catalysts," *Nature chemistry,* vol. 1, no. 1, pp. 37-46, 2009.

[78]   N. S. Allen, N. Mahdjoub, V. Vishnyakov, P. J. Kelly, and R. J. Kriek, "The effect of crystalline phase (anatase, brookite and rutile) and size on the photocatalytic activity of

calcined polymorphic titanium dioxide (TiO_2)," *Polymer degradation and stability,* vol. 150, pp. 31-36, 2018.

[79] Y. Wu, F. Gao, H. Wang, L. Kovarik, B. Sudduth, and Y. Wang, "Probing acid–base properties of anatase TiO_2 nanoparticles with dominant {001} and {101} facets using methanol chemisorption and surface reactions," *The Journal of Physical Chemistry C,* vol. 125, no. 7, pp. 3988-4000, 2021.

[80] H. Pan, B. Gu, and Z. Zhang, "Phase-dependent photocatalytic ability of TiO_2: a first-principles study," *Journal of Chemical Theory and Computation,* vol. 5, no. 11, pp. 3074-3078, 2009.

[81] Z. Goren, I. Willner, A. Nelson, and A. Frank, "Selective photoreduction of carbon dioxide/bicarbonate to formate by aqueous suspensions and colloids of palladium-titania," *Journal of Physical Chemistry,* vol. 94, no. 9, pp. 3784-3790, 1990.

[82] K. Mori, T. Sano, H. Kobayashi, and H. Yamashita, "Surface engineering of a supported PdAg catalyst for hydrogenation of CO_2 to formic acid: elucidating the active Pd atoms in alloy nanoparticles," *Journal of the American Chemical Society,* vol. 140, no. 28, pp. 8902-8909, 2018.

[83] G. Calleja, D. P. Serrano, R. Sanz, P. Pizarro, and A. García, "Study on the synthesis of high-surface-area mesoporous TiO_2 in the presence of nonionic surfactants," *Industrial & engineering chemistry research,* vol. 43, no. 10, pp. 2485-2492, 2004.

[84] X. Wang, X. Zou, Z. Rui, Y. Wang, and H. Ji, "Highly dispersed and active Pd nanoparticles over titania support through engineering oxygen vacancies and their anchoring effect," *AIChE Journal,* vol. 66, no. 8, p. e16288, 2020.

[85] P. E. Blöchl, "Projector augmented-wave method," *Physical review B,* vol. 50, no. 24, p. 17953, 1994.

[86] G. Kresse and D. Joubert, "From ultrasoft pseudopotentials to the projector augmented-wave method," *Physical review b,* vol. 59, no. 3, p. 1758, 1999.

[87] G. Kresse and J. Furthmüller, "Efficiency of ab-initio total energy calculations for metals and semiconductors using a plane-wave basis set," *Computational materials science,* vol. 6, no. 1, pp. 15-50, 1996.

[88] G. Kresse and J. Hafner, "Ab initio molecular dynamics for liquid metals," *Physical review B,* vol. 47, no. 1, p. 558, 1993.

[89] G. Kresse and J. Hafner, "Ab initio molecular-dynamics simulation of the liquid-metal–amorphous-semiconductor transition in germanium," *Physical Review B,* vol. 49, no. 20, p. 14251, 1994.

[90] G. Kresse and J. Furthmüller, "Efficient iterative schemes for ab initio total-energy calculations using a plane-wave basis set," *Physical review B,* vol. 54, no. 16, p. 11169, 1996.

[91] "A consistent and accurate ab initio parametrization of density functional dispersion correction (DFT-D) for the 94 elements H-Pu," *The Journal of Chemical Physics,* vol. 132, no. 15, p. 154104, 2010, doi: 10.1063/1.3382344.

[92] Z. Hu and H. Metiu, "Choice ofUfor DFT+UCalculations for Titanium Oxides," *The Journal of Physical Chemistry C,* vol. 115, no. 13, pp. 5841-5845, 2011, doi: 10.1021/jp111350u.

[93] G. J. de AA Soler–Illia and C. Sanchez, "Interactions between poly (ethylene oxide)-based surfactants and transition metal alkoxides: their role in the templated construction of

mesostructured hybrid organic–inorganic composites," *New Journal of Chemistry,* vol. 24, no. 7, pp. 493-499, 2000.

[94]   G. J. de AA Soler-Illia, E. Scolan, A. Louis, P.-A. Albouy, and C. Sanchez, "Design of meso-structured titanium oxo based hybrid organic–inorganic networks," *New Journal of Chemistry,* vol. 25, no. 1, pp. 156-165, 2001.

[95]   A. Soloviev, R. Tufeu, C. Sanchez, and A. Kanaev, "Nucleation Stage in the Ti (OPr i) 4 Sol− Gel Process," *The Journal of Physical Chemistry B,* vol. 105, no. 19, pp. 4175-4180, 2001.

[96]   M. Schneider and A. Baiker, "Titania-based aerogels," *Catalysis Today,* vol. 35, no. 3, pp. 339-365, 1997.

[97]   L. Campbell, B. Na, and E. Ko, "Synthesis and characterization of titania aerogels," *Chemistry of materials,* vol. 4, no. 6, pp. 1329-1333, 1992.

[98]   H. Kominami *et al.*, "Thermal treatment of titanium alkoxides in organic media: novel synthesis methods for titanium (IV) oxide photocatalyst of ultra-high activity," in *Studies in Surface Science and Catalysis*, vol. 130: Elsevier, 2000, pp. 1937-1942.

[99]   P. Alexandridis and K. Andersson, "Effect of solvent quality on reverse micelle formation and water solubilization by poly (ethylene oxide)/poly (propylene oxide) and poly (ethylene oxide)/poly (butylene oxide) block copolymers in xylene," *Journal of colloid and interface science,* vol. 194, no. 1, pp. 166-173, 1997.

[100]   N. Jain, V. Aswal, P. Goyal, and P. Bahadur, "Salt induced micellization and micelle structures ofˈPEO/PPO/PEO block copolymers in aqueous solution," *Colloids and Surfaces A: Physicochemical and Engineering Aspects,* vol. 173, no. 1-3, pp. 85-94, 2000.

[101] P. Desai, N. Jain, and P. Bahadur, "Anomalous clouding behavior of an ethylene oxide–propylene oxide block copolymer in aqueous solution," *Colloids and Surfaces A: Physicochemical and Engineering Aspects,* vol. 197, no. 1-3, pp. 19-26, 2002.

[102] P. Yang, D. Zhao, D. I. Margolese, B. F. Chmelka, and G. D. Stucky, "Generalized syntheses of large-pore mesoporous metal oxides with semicrystalline frameworks," *Nature,* vol. 396, no. 6707, pp. 152-155, 1998.

[103] P. Yang, D. Zhao, D. I. Margolese, B. F. Chmelka, and G. D. Stucky, "Block copolymer templating syntheses of mesoporous metal oxides with large ordering lengths and semicrystalline framework," *Chemistry of Materials,* vol. 11, no. 10, pp. 2813-2826, 1999.

[104] V. G. Deshmane and Y. G. Adewuyi, "Synthesis and kinetics of biodiesel formation via calcium methoxide base catalyzed transesterification reaction in the absence and presence of ultrasound," *Fuel,* vol. 107, pp. 474-482, 2013.

[105] D. Huang, Y. Wang, L. Yang, and G. Luo, "Direct synthesis of mesoporous TiO_2 modified with phosphotungstic acid under template-free condition," *Microporous and mesoporous materials,* vol. 96, no. 1-3, pp. 301-306, 2006.

[106] V. G. Deshmane and Y. G. Adewuyi, "Mesoporous nanocrystalline sulfated zirconia synthesis and its application for FFA esterification in oils," *Applied Catalysis A: General,* vol. 462, pp. 196-206, 2013.

[107] F. Lin *et al.*, "Single-facet dominant anatase TiO_2 (101) and (001) model catalysts to elucidate the active sites for alkanol dehydration," *ACS Catalysis,* vol. 10, no. 7, pp. 4268-4279, 2020.

[108] M. Lazzeri, A. Vittadini, and A. Selloni, "Structure and energetics of stoichiometric TiO_2 anatase surfaces," *Physical Review B,* vol. 63, no. 15, p. 155409, 2001.

[109] M. Lazzeri, A. Vittadini, and A. Selloni, "Erratum: Structure and energetics of stoichiometric TiO_2 anatase surfaces (Physical Review B (2001) 63 (155409))," *Physical Review B-Condensed Matter and Materials Physics,* vol. 65, no. 11, p. 011990, 2002.

[110] Z. Wang, R. Lin, Y. Huo, H. Li, and L. Wang, "Formation, detection, and function of oxygen vacancy in metal oxides for solar energy conversion," *Advanced Functional Materials,* vol. 32, no. 7, p. 2109503, 2022.

[111] S. Yamamoto *et al.*, "Water adsorption on α-Fe2O3 (0001) at near ambient conditions," *The Journal of Physical Chemistry C,* vol. 114, no. 5, pp. 2256-2266, 2010.

[112] B. Rusinque, S. Escobedo, and H. de Lasa, "Photoreduction of a Pd-doped mesoporous TiO2 photocatalyst for hydrogen production under visible light," *Catalysts,* vol. 10, no. 1, p. 74, 2020.

[113] C. M. Mendez, H. Olivero, D. E. Damiani, and M. A. Volpe, "On the role of Pd β-hydride in the reduction of nitrate over Pd based catalyst," *Applied Catalysis B: Environmental,* vol. 84, no. 1-2, pp. 156-161, 2008.

[114] F. Cao *et al.*, "Size-Controlled Synthesis of Pd Nanocatalysts on Defect-Engineered CeO2 for CO2 Hydrogenation," *ACS Applied Materials & Interfaces,* vol. 13, no. 21, pp. 24957-24965, 2021.

[115] Z. Chen, F.-X. Cao, W. Gao, Q.-C. Dong, and Y.-Q. Qu, "Uniform small metal nanoparticles anchored on CeO_2 nanorods driven by electroless chemical deposition," *Rare Metals,* vol. 39, pp. 806-814, 2020.

[116] S. Zhang *et al.*, "Towards highly active Pd/CeO_2 for alkene hydrogenation by tuning Pd dispersion and surface properties of the catalysts," *Nanoscale,* vol. 9, no. 9, pp. 3140-3149, 2017.

[117] H. Tan, J. Wang, S. Yu, and K. Zhou, "Support morphology-dependent catalytic activity of Pd/CeO2 for formaldehyde oxidation," *Environmental science & technology,* vol. 49, no. 14, pp. 8675-8682, 2015.

[118] Y. Guo *et al.*, "Low-temperature CO_2 methanation over CeO_2-supported Ru single atoms, nanoclusters, and nanoparticles competitively tuned by strong metal–support interactions and H-spillover effect," *ACS catalysis,* vol. 8, no. 7, pp. 6203-6215, 2018.

[119] S. A. Singh, K. Vishwanath, and G. Madras, "Role of hydrogen and oxygen activation over Pt and Pd-doped composites for catalytic hydrogen combustion," *ACS Applied Materials & Interfaces,* vol. 9, no. 23, pp. 19380-19388, 2017.

[120] U. Aschauer and A. Selloni, "Hydrogen interaction with the anatase TiO_2 (101) surface," *Physical Chemistry Chemical Physics,* vol. 14, no. 48, pp. 16595-16602, 2012.

[121] Y.-F. Li, U. Aschauer, J. Chen, and A. Selloni, "Adsorption and reactions of O_2 on anatase TiO2," *Accounts of chemical research,* vol. 47, no. 11, pp. 3361-3368, 2014.

[122] H. Cheng and A. Selloni, "Surface and subsurface oxygen vacancies in anatase TiO_2 and differences with rutile," *Physical Review B,* vol. 79, no. 9, p. 092101, 2009.

[123] H. Cheng and A. Selloni, "Energetics and diffusion of intrinsic surface and subsurface defects on anatase TiO_2 (101)," *The Journal of chemical physics,* vol. 131, no. 5, p. 054703, 2009.

[124] Y. He, O. Dulub, H. Cheng, A. Selloni, and U. Diebold, "Evidence for the predominance of subsurface defects on reduced anatase TiO_2 (101)," *Physical Review Letters,* vol. 102, no. 10, p. 106105, 2009.

[125] F. Gunkel, D. V. Christensen, Y. Chen, and N. Pryds, "Oxygen vacancies: The (in) visible friend of oxide electronics," *Applied physics letters,* vol. 116, no. 12, p. 120505, 2020.

[126] R. Merkle and J. Maier, "How is oxygen incorporated into oxides? A comprehensive kinetic study of a simple solid-state reaction with $SrTiO_3$ as a model material," *Angewandte Chemie International Edition,* vol. 47, no. 21, pp. 3874-3894, 2008.

[127] H. Li and L. Zhang, "Oxygen vacancy induced selective silver deposition on the {001} facets of BiOCl single-crystalline nanosheets for enhanced Cr (VI) and sodium pentachlorophenate removal under visible light," *Nanoscale,* vol. 6, no. 14, pp. 7805-7810, 2014.

[128] M. Kong *et al.*, "Tuning the relative concentration ratio of bulk defects to surface defects in TiO2 nanocrystals leads to high photocatalytic efficiency," *Journal of the American Chemical Society,* vol. 133, no. 41, pp. 16414-16417, 2011.

[129] Y. Huang, W. Wang, Y. Zhang, J. Cao, R. Huang, and X. Wang, "Synthesis and applications of nanomaterials with high photocatalytic activity on air purification," in *Novel Nanomaterials for Biomedical, Environmental and Energy Applications*: Elsevier, 2019, pp. 299-325.

[130] R. Prins, "Hydrogen spillover. Facts and fiction," *Chemical reviews,* vol. 112, no. 5, pp. 2714-2738, 2012.

[131] Y. Wang, F. Wang, Q. Song, Q. Xin, S. Xu, and J. Xu, "Heterogeneous ceria catalyst with water-tolerant Lewis acidic sites for one-pot synthesis of 1, 3-diols via Prins condensation and hydrolysis reactions," *Journal of the American Chemical Society,* vol. 135, no. 4, pp. 1506-1515, 2013.

[132] F. Joó, L. Nádasdi, J. Elek, and G. Laurenczy, "Homogeneous hydrogenation of aqueous hydrogen carbonate to formate under exceedingly mild conditions—a novel possibility of carbon dioxide activation," *Chemical Communications,* no. 11, pp. 971-972, 1999.

[133]   T. K. Slot, N. Riley, N. R. Shiju, J. W. Medlin, and G. Rothenberg, "An experimental approach for controlling confinement effects at catalyst interfaces," *Chemical science,* vol. 11, no. 40, pp. 11024-11029, 2020.

[134]   Z. Dong *et al.*, "Efficient Pd on carbon catalyst for ammonium formate dehydrogenation: Effect of surface oxygen functional groups," *Applied Catalysis B: Environmental,* vol. 321, p. 122015, 2023.

APPENDIX

Appendix A: Standard operating procedure for H_2 – TPR analysis

Steps	Components		Conditions
Experiments	Preparation		Ar
	Carrier		10% H_2/Ar
	Loop		None
	Valves		Trap – Prepare – Fill – Bypass
Temperature Ramp	Temperature		300 ºC
	Rate		10 ºC/min
	Hold		30 min
	Cool		No
Temperature Ramp	Return to ambient		
Change Gas Flows	Preparation		None
	Carrier		10% H_2/Ar
	Loop		None
Wait	Until baseline is stable		
Start Recording	Record after every 1 second		
Wait	5 min		
Temperature Ramp	Temperature		900 ºC
	Rate		10 ºC/min
	Hold		15 min
	Cool		No
Stop Recording			

Steps	Components	Conditions
Done	*Return to ambient*	Yes
	Enable Kwik cool	No
	Leave the detector enable	Off
	Preparation	Non
	Carrier	Ar
	Loop	None
	Valves	Bypass – Prepare – Fill – Bypass

Appendix B: Standard operating procedure for OSC pulse chemisorption analysis

Steps	Components	Conditions
Experiments	*Preparation*	He
	Carrier	He
	Loop	None
	Valves	Trap – Prepare – Fill – Bypass
Temperature Ramp	*Temperature*	400 ºC
	Rate	10 ºC/min
	Hold	30 min
	Cool	No
Temperature Ramp	*Temperature*	500 ºC
	Rate	20 ºC/min
	Hold	5 min
	Cool	No

Change Gas Flows	*Preparation*	He
	Carrier	He
	Loop	10% O_2/He
	Valves	Trap – Analyze – Fill – Bypass
Wait	Until baseline is stable	
Start Recording	Record after every 0.5 second	
Wait	10 min	
Start Repeat	20 times	
Dose	Inject loop gas Wait for change from baseline or 2 minutes then return to baseline	
Stop Repeat		
Stop Recording		
Done	*Return to ambient*	Yes
	Enable Kwik cool	No
	Leave the detector enable	Off
	Preparation	Non
	Carrier	He
	Loop	None
	Valves	Bypass – Prepare – Fill – Bypass

Appendix C: Standard operating procedure for O_2 – TPD analysis

Steps	Components	Conditions
Experiments	*Preparation*	He
	Carrier	He
	Loop	None
	Valves	Bypass – Prepare – Fill – Bypass
Temperature Ramp	*Temperature*	200 ºC
	Rate	10 ºC/min
	Hold	60 min
	Cool	No
Experiments	*Preparation*	He
	Carrier	He
	Loop	None
	Valves	Bypass – Prepare – Fill – Bypass
Temperature Ramp	Return to ambient	
Change Gas Flows	*Preparation*	10% O_2/He
	Carrier	He
	Loop	10% O_2/He
	Valves	Bypass – Prepare – Fill – Bypass
Wait	60 minutes	
Wait	Until baseline is stable	
Start Recording	Record after every 1 second	

Temperature Ramp	*Temperature*	900 ºC
	Rate	10 ºC/min
	Hold	0 min
	Cool	No
Wait	10 min	
Temperature Ramp	Return to ambient	
Done	*Return to ambient*	Yes
	Enable Kwik cool	No
	Leave the detector enable	Off
	Preparation	Non
	Carrier	He
	Loop	None
	Valves	Bypass – Prepare – Fill – Bypass

Appendix D: Standard operating procedure for H_2 – TPD analysis

Steps	Components	Conditions
Experiments	*Preparation*	Ar
	Carrier	Ar
	Loop	None
	Valves	Bypass – Prepare – Fill – Bypass
Temperature Ramp	*Temperature*	300 ºC
	Rate	50 ºC/min

	Hold	10 min
	Cool	No
Experiments	*Preparation*	Ar
	Carrier	Ar
	Loop	None
	Valves	Bypass – Prepare – Fill – Bypass
Temperature Ramp	Return to ambient	
Change Gas Flows	*Preparation*	10% H_2/Ar
	Carrier	Ar
	Loop	10% H_2/Ar
	Valves	Bypass – Prepare – Fill – Bypass
Wait	60 minutes	
Change Gas Flows	*Preparation*	None
	Carrier	Ar
	Loop	10% H_2/Ar
	Valves	Bypass – Analyze – Fill – Bypass
Wait	30 minutes	
Wait	Until baseline is stable	
Start Recording	Record after every 1 second	
Temperature Ramp	*Temperature*	900 ºC
	Rate	10 ºC/min
	Hold	0 min

		Cool	No
Wait		30 min	
Stop Recording			
Temperature Ramp		Return to ambient	
Done		Return to ambient	Yes
		Enable Kwik cool	No
		Leave the detector enable	Off
		Preparation	Non
		Carrier	Ar
		Loop	None
		Valves	Bypass – Prepare – Fill – Bypass

Appendix E: List of Publications

Below is a list of publications I had the pleasure of contributing to:

- Zhun Dong, Ahmad Mukhtar, Thomas Ludwig, Sneha A. Akhade, ShinYoung Kang, Brandon Wood, Katarzyna Grubel, Mark Engelhard, Tom Autrey, and Hongfei Lin. "Efficient Pd on carbon catalyst for ammonium formate dehydrogenation: Effect of surface oxygen functional groups." *Applied Catalysis B: Environmental* 321 (2023): 122015. https://doi.org/10.1016/j.apcatb.2022.122015.

- Zhun Dong, Ahmad Mukhtar, and Hongfei Lin. "Heterogeneous catalysis on liquid organic hydrogen carriers." *Topics in Catalysis* 64, no. 7-8 (2021): 481-508. https://doi.org/10.1007/s11244-021-01458-5

- Ahmad Mukhtar, Sidra Saqib, Jangam Ashok, Zhun Dong, Mark Bowden, Mark Engelhard, Katarzyna Grubel, Tom Autrey, Hongfei Lin, "Highly Active and Stable Pd Nanoparticles Supported Over Defective Mesoporous TiO_{2-x} for Bicarbonate-Formate System: Role of H_2 Spillover and Oxygen Vacancies", Drafting.

- Zhun Dong, Ahmad Mukhtar, Thomas Ludwig, Sneha A. Akhade, Wenda Hu, Jian Zhi Hu, Katarzyna Grubel, Mark Engelhard, Tom Autrey, Hongfei Lin, "Carbon-supported Pd-Ag bimetallic catalyst with exceptional activity for ammonium formate dehydrogenation", *Catalysis Science and Technology*, Submitted.